# Fixed points, stable manifolds, weather regimes, and their predictability

Bruno Deremble, Fabio D'Andrea, and Michael Ghil[a)]
*Laboratoire de Météorologie Dynamique (CNRS and IPSL), Ecole Normale Supérieure, 75231 Paris Cedex 05, France*

(Received 9 March 2009; accepted 19 August 2009; published online 27 October 2009)

In a simple, one-layer atmospheric model, we study the links between low-frequency variability and the model's fixed points in phase space. The model dynamics is characterized by the coexistence of multiple "weather regimes." To investigate the transitions from one regime to another, we focus on the identification of stable manifolds associated with fixed points. We show that these manifolds act as separatrices between regimes. We track each manifold by making use of two local predictability measures arising from the meteorological applications of nonlinear dynamics, namely, "bred vectors" and singular vectors. These results are then verified in the framework of ensemble forecasts issued from "clouds" (ensembles) of initial states. The divergence of the trajectories allows us to establish the connections between zones of low predictability, the geometry of the stable manifolds, and transitions between regimes. © *2009 American Institute of Physics*. [doi:10.1063/1.3230497]

**Multiple fixed points, or multiple "equilibria," are a ubiquitous manifestation of nonlinearity and chaos. These multiple equilibria are often associated, in turn, with multiple regimes of behavior: the system trajectory dwells for extended time intervals in the vicinity of two or more unstable equilibria, and each such vicinity exhibits spatiotemporal features that characterize the corresponding regime.[8,41] This paper highlights the role played by the stable manifold of a centrally located fixed point in separating multiple regimes in a simple atmospheric model.[8] Local predictability is calculated by several methods used in dynamic meteorology and numerical weather prediction and related to the numerically simulated divergence of model trajectories. The results are discussed in terms of observed behavior of atmospheric flows, on the one hand, and explained in terms of even simpler models, including the Lorenz[44] model, on the other. We believe that these results can be extended to more detailed and realistic climate models, as well as to other application areas of nonlinear dynamics.[24]**

## I. INTRODUCTION

### A. Background

The pioneering work of Lorenz[44,46] has led to the realization that the atmosphere is a chaotic system, and thus has a finite predictability time. The predictability limit depends on which specific phenomenon we are considering, as well as on the application envisaged for the prediction. While a thunderstorm can be predicted only a few hours before its occurrence, other phenomena have longer time scales, e.g., the Madden–Julian oscillation[52,53] that has a time scale around 40 days or the El Niño/Southern Oscillation (ENSO), with its seasonal-to-interannual time scale.[65]

During the past three decades, considerable research has been performed on atmospheric variability with a time scale from a week up to a few months and on its predictability. Phenomena that occur on such a time scale are grouped under the label of low-frequency variability (LFV). Their dynamics can be described by the existence of preferred flow patterns (or "regimes"), whose frequency of appearance and/or persistence corresponds to that time scale.

Several authors (e.g., Refs. 24 and 41) have hypothesized that the flow regimes constitute more predictable phases of the large-scale atmospheric flow evolution and could be used to extend the predictability, conditioned on passage through such a persistent regime. A key aspect of studies proceeding from this hypothesis is the identification of the regimes. This identification is often associated with the search for subsets of the phase space in which the system spends longer time intervals. Increasingly objective and sophisticated statistical methods for identifying and describing these regimes have been used in the literature.[3,30,37,57,58,74]

Another way to look at the regimes relies on more dynamical criteria and attempts to establish a correspondence between them and stable or unstable fixed points of the flow in its phase space. Indeed the presence of stable and unstable fixed points can influence greatly the trajectories by repelling or attracting them.

The study of such "multiple equilibria" has largely, but not exclusively, concentrated on low-dimensional models; see Refs. 8, 10, 12–15, 35, 41, 45, and 68 all of which considered models of dimension no higher than 25. While a few atmospheric papers (e.g., Refs. 32 and 39) and several oceanographic ones (e.g., Refs. 19, 34, 66, 67, 72, and 73) addressed multiple equilibria and their stability in so-called intermediate models with hundreds to many thousands of discrete variables, this approach can still not be easily generalized to full-blown general circulation models (GCMs), with millions of discrete variables.

The presence of multiple regimes in atmospheric LFV is still a matter of debate.[24,48,54,59,75] Thus, Sardeshmukh *et al.*[70]

[a)]Electronic mail: ghil@lmd.ens.fr. Also at the Department of Atmospheric and Oceanic Sciences and Institute of Geophysics and Planetary Physics, University of California, Los Angeles, CA 90095-1565.

 

and Sura *et al.*,[76] for instance, argued that the observed non-Gaussian probability distribution function (PDF) of past "weather maps" in a suitably defined phase space does not necessarily imply the existence of persistent flow patterns that arise from nonlinear dynamics. They showed that such PDFs can be reproduced by simple systems governed by linear dynamics but subject to multiplicative noise. Deloncle *et al.*[16] and Kondrashov *et al.*,[38] however, demonstrated that the transition paths between the regimes are consistent with nonlinear, deterministic dynamics rather than linear stochastic dynamics.

### B. Our study

In this study, we use a by now classical model of atmospheric flow over simplified topography, due to Charney and Devore.[8] This barotropic, low-order model has been extensively used in the past and it produces multiple equilibria, as well as periodic and chaotic solutions that simulate large-scale atmospheric dynamics. A set of parameters is found for which one can identify flow regimes visually. The regimes are associated with different space and time scales of variation. In this sense, they represent the multiplicity of scales present in Earth's atmosphere. When interested in phenomena on the time scales of days to months, the atmosphere is characterized by high-frequency baroclinic transients, interacting with the slower and larger scales that characterize its LFV.

We will illustrate the link between the regimes and their predictability using several tools of nonlinear dynamics. To do so, we will analyze the local properties of the flow in phase space in order to be able to predict a possible regime change. Pursuing the idea that the system's dynamics is linked to the position and stability of its fixed points, we will devote particular attention to one specific hyperbolic point of the Charney and Devore (CDV) system and study the invariant manifolds of that point. In fact, convergence and divergence of the system's trajectories occur along these manifolds, which can play the role of separatrices between different regions in phase space.

In both statistical and dynamical studies of atmospheric LFV, it is common to consider subspaces of lower dimension. We use this device here only for visualization purposes, relying on the customary basis vectors provided by principal component analysis of the model output. These vectors are called empirical orthogonal functions (EOFs) (Ref. 43) in the atmospheric dynamics community, and the reduction used here is by projection onto the leading EOFs, as usual.

Operational forecasting centers are fully aware of the dependence of the predictability of weather on the specific initial state. To explore the phase space of the numerical weather prediction model in the neighborhood of the initial state for a given day, each center performs an ensemble of forecasts, starting from a set of perturbed initial data; see Toth and Kalnay,[78] Molteni *et al.*,[60] and Houtekamer *et al.*[33]). The spread of the ensemble over the days into the forecast is an indication of its reliability, i.e., of the predictability of the weather on that particular day.

The purpose of the present paper is to provide insight into the way that this conditional predictability may depend on the position and stability of the system's invariant manifolds. To examine this issue, we will be using here some of the local predictability measures that have been recently used by weather forecasting centers, namely "bred vectors" (BVs), introduced by Toth and Kalnay,[78,79] and singular vectors (SVs), as described by Buizza and Palmer.[5]

These two kinds of dynamical tools differ in their properties[42] and have both already been used in order to predict regime transitions. Corti and Palmer[11] showed how irregular a trajectory that leaves one regime to reach another one may be: the addition of a small perturbation to the initial state can cancel, under certain conditions, the transition. Evans *et al.*[21] used the growth rate of the BVs to predict a regime change in the Lorenz[44] model.

The outline of this paper is as follow: Section II is a brief description of the CDV model. We recall the formulation of the model and specify the range of parameters for which it will be used; details are provided in Appendix A. In the same section we also introduce BVs and SVs. Section III is a short analysis and description of the CDV model's phase-space behavior. The fixed points and their stability are computed and represented in the subspace of the leading EOFs. We also show how certain fixed points can be associated with a regime. In Sec. IV we use BVs and SVs to approximate the stable and unstable manifolds of a centrally located fixed point and to define regions of low predictability, i.e., regions where a change of regime is probable. Section V verifies the localization of the low-predictability areas computed above by directly performing ensemble integrations of the model. A summary and discussion follow in Sec. VI.

In Appendixes B and C, we use two even simpler models to illustrate and clarify further the results obtained with the CDV model. Their behavior exhibits some noteworthy similarities with the CDV model in the parameter range of interest. The first one is Hamiltonian and resembles the elastic pendulum; see Lynch.[51] This model represents an "artist's view" of the atmosphere and it is well suited for studying the multiple-regime paradigm. In it, we are able to reproduce analytically the results obtained numerically for the CDV model. In Appendix C, we show that the present results hold for the Lorenz[44] model as well.

## II. MODEL AND METHODS

In this section, we describe the main model under study and the two local predictability measures on which we concentrate. The CDV (Ref. 8) model simulates a barotropic atmosphere in which an externally forced jet interacts nonlinearly with the topography. For completeness and consistency, we summarize here the derivation of the model equations. The full description of the model can be found in Appendix A. We also introduce the BVs and SVs. The reader who is familiar with either the CDV model or the tools of analysis can proceed directly to Sec. III.

### A. Model description

The model is governed by the quasigeostrophic equation of potential vorticity for a fluid evolving in a rectangular channel of dimension $2\pi L \times \pi L$. This channel is located on a $\beta$-plane[23] and has a free surface of height $H+\eta$ (see Appendix A for further details):

$$\partial_t\left(\nabla^2\psi - \frac{\psi}{\lambda^2}\right) + J\left(\psi, \nabla^2\psi - \frac{\psi}{\lambda^2} + f_0\frac{h}{H} + \beta y\right) = -\frac{f_0 D_E}{2H}\nabla^2(\psi - \psi^*). \quad (1)$$

Here $\psi$ is the streamfunction of the velocity field, $f_0$ and $\beta$ are parameters associated with the Coriolis force, $h$ is the topography at the bottom of the $\beta$-channel, $\lambda$ is the Rossby radius of deformation, $H$ is the mean height of the fluid, and $D_E$ is the Ekman layer depth.

We first nondimensionalize this equation and expand it in the eigenfunctions $F_i$ of the Laplacian operator by setting

$$(\psi, h, \psi^*) = \sum_{i=1}^{N} (\psi_i, h_i, \psi_i^*)F_i. \quad (2)$$

We truncate this expansion in order to retain only $N=6$ modes. The topographic profile chosen by CDV—based on the midlatitude topography of the northern hemisphere first used by Charney and Eliassen[9]—only projects on the second mode, so that $h=h_0F_2$. Furthermore, we will study the model considering only a zonal, west-east forcing, $\psi^*=\psi_1^*F_1$ (see Appendix A). We thus obtain the system of ordinary differential equations:

$$\begin{aligned}
\dot{\psi}_1 &= -k_{01}(\psi_1 - \psi_1^*) + h_{01}\psi_3,\\
\dot{\psi}_2 &= -k_{n1}\psi_2 - (\alpha_{n1}\psi_1 - \beta_{n1})\psi_3 - \delta_{n1}\psi_4\psi_6,\\
\dot{\psi}_3 &= -k_{n1}\psi_3 + (\alpha_{n1}\psi_1 - \beta_{n1})\psi_2 - h_{n1}\psi_1 + \delta_{n1}\psi_4\psi_5,\\
\dot{\psi}_4 &= -k_{02}\psi_4 + \epsilon_n(\psi_2\psi_6 - \psi_3\psi_5) + h_{02}\psi_6,\\
\dot{\psi}_5 &= -k_{n2}\psi_5 - (\alpha_{n2}\psi_1 - \beta_{n2})\psi_6 - \delta_{n2}\psi_4\psi_3,\\
\dot{\psi}_6 &= -k_{n2}\psi_6 + (\alpha_{n2}\psi_1 - \beta_{n2})\psi_5 - h_{n2}\psi_4 + \delta_{n2}\psi_4\psi_1.
\end{aligned} \quad (3)$$

Following Charney and Devore and Ref. 23 we consider $\psi_1^*$ as this model's main bifurcation parameter and keep here the other parameters as fixed. The dimensional height of the topography is set to 4000 m and the beta effect is adjusted so as to linearize the Coriolis force about a midchannel axis placed at 45° N.

### B. Local predictability measures

Let us write the six equations in Eq. (3) in a more compact form,[41]

$$\dot{\boldsymbol{\Psi}} = \boldsymbol{F}(\boldsymbol{\Psi}(t)), \quad (4)$$

with $\boldsymbol{\Psi}=(\psi_1, \psi_2, \ldots, \psi_6)$ and $\boldsymbol{F}$ a nonlinear, time-independent operator of dimension 6. Local predictability is quantified by the separation of two trajectories that are initially close at time $t_0$. For two vectors $\boldsymbol{\Psi}(t)$ and $\boldsymbol{\Psi}'(t)$, both solutions of Eq. (4), we call $\boldsymbol{\delta\Psi}(t)=\boldsymbol{\Psi}'(t)-\boldsymbol{\Psi}(t)$ a perturbation to $\boldsymbol{\Psi}(t)$ at time $t$. Local predictability can be measured using the expansion rate of the two solutions between $t_0$ and $t_1$: $\|\boldsymbol{\delta\Psi}(t_1)\|/\|\boldsymbol{\delta\Psi}(t_0)\|$, $\|\cdot\|$ being a quadratic norm associated with the inner product $(\cdot,\cdot)$; typically one uses the $L_2$ norm, also called the root-mean-square distance between two state vectors $\boldsymbol{\Psi}_1$ and $\boldsymbol{\Psi}_2$.

Among several different ways to estimate this expansion rate, we rely on two widely used ones. Essentially, a linear way to study the divergence of trajectories is given by SVs, while a more nonlinear one is given by BVs.

#### 1. Bred vectors

BVs have been formulated and implemented in operational practice by Toth and Kalnay[78,79] at the U.S. National Centers for Environmental Prediction. The original idea was to construct an ensemble of optimal perturbation in order to carry out an ensemble forecast by selecting the most important growing error.

This essentially nonlinear and computationally very simple method consists in the following steps:

- add to the initial state $\boldsymbol{\Psi}(t_0)$ a small random perturbation $\boldsymbol{\delta\Psi}(t_0)$ and obtain a perturbed initial state $\boldsymbol{\Psi}'(t_0)$;
- integrate the model from both the unperturbed and the perturbed initial state for a given time $T=(t_1-t_0)$;
- measure the difference $\|\boldsymbol{\delta\Psi}(t_1)\|$ between the two trajectories and rescale this difference to have the same size as the initial perturbation $\|\boldsymbol{\delta\Psi}(t_0)\|$;
- add this new perturbation to the "control run" $\boldsymbol{\Psi}(t_1)$;
- restart from the second step.

After several rescalings, the perturbation evolves toward the fastest-growing error direction. The method thus "breeds" the nonlinear perturbation that grows fastest.

The key quantity resulting from this procedure is the growth rate,

$$G_{\mathrm{BV}}(\boldsymbol{\Psi}(t_0), T) \equiv \frac{1}{T}\log\left(\frac{\|\boldsymbol{\delta\Psi}(t_1)\|}{\|\boldsymbol{\delta\Psi}(t_0)\|}\right). \quad (5)$$

The leading BV obtained will help us identify the sensitive trajectories for which the error growth is high, as well as the relatively stable trajectories for which this rate is small.

#### 2. Singular vectors

The SVs describe the evolution of small perturbations that are governed by the linearized version of Eq. (4). The time evolution of an infinitesimal perturbation $\boldsymbol{\delta\Psi}(t)$ to the flow $\boldsymbol{\Psi}(t)$ is governed by the linearization of Eq. (4) about the trajectory $\boldsymbol{\Psi}(t)$,

$$\boldsymbol{\delta\dot{\Psi}}(t) = \boldsymbol{J}(\boldsymbol{\Psi}(t)) \cdot \boldsymbol{\delta\Psi}(t). \quad (6)$$

Here $\boldsymbol{J}(\boldsymbol{\Psi}(t))$ is the Jacobian matrix defined as

$$\boldsymbol{J}_{ij}(\boldsymbol{\Psi}(t)) = \left.\frac{\partial \boldsymbol{F}_i(X)}{\partial X_j}\right|_{X=\boldsymbol{\Psi}(t)}. \quad (7)$$

We call $\mathcal{L}(t,t_0)$ the solution of the tangent linear equation,

$$\dot{\mathcal{L}}(t,t_0) = \boldsymbol{J}(\boldsymbol{\Psi}(t)) \cdot \mathcal{L}(t_0,t_0). \tag{8}$$

Taking as initial condition in Eq. (8) $\mathcal{L}(t_0,t_0)=Id$, one then obtains

$$\boldsymbol{\delta\Psi}(t_1) = \mathcal{L}(t_1,t_0) \cdot \boldsymbol{\delta\Psi}(t_0), \tag{9}$$

where $\mathcal{L}$ is called the linear propagator from $t_0$ to $t_1$. Hence, one can write the following equalities:

$$\frac{\|\boldsymbol{\delta\Psi}(t_1)\|}{\|\boldsymbol{\delta\Psi}(t_0)\|} = \frac{\|\mathcal{L}(t_1,t_0)\boldsymbol{\delta\Psi}(t_0)\|}{\|\boldsymbol{\delta\Psi}(t_0)\|} = \frac{(\boldsymbol{\delta\Psi}(t_0)\mathcal{L}^*(t_1,t_0),\mathcal{L}(t_1,t_0)\boldsymbol{\delta\Psi}(t_0))^{1/2}}{\|\boldsymbol{\delta\Psi}(t_0)\|}, \tag{10}$$

with $\mathcal{L}^*$ denoting the adjoint operator of our propagator $\mathcal{L}$. The eigenvectors of the normal operator $\mathcal{L}^*(t_1,t_0)\cdot\mathcal{L}(t_1,t_0)$ optimize the growth of the perturbation for the norm chosen herein and for the time interval $T=(t_1-t_0)$.

The maximal possible growth rate is given by the first singular value $S_1$ of $\mathcal{L}(t_1,t_0)$, i.e., by the first eigenvalue of the associated normal operator. In the limit of $T\to\infty$, the Oseledec[62] theorem guarantees the convergence of

$$G_{\mathrm{SV}} \equiv (1/T)\log(S_1) \tag{11}$$

toward the first Lyapunov exponent.

Unlike the BV growth rate of Eq. (5), the singular-value decomposition of the normal operator thus yields a theoretical expansion rate (11) that corresponds for large $T$ to the maximum expansion rate possible. The drawback of the SV approach for the small $T$ we are interested in when studying local predictability is the need to carry out, at least in part, the much more costly singular-value decomposition of the normal operator. In the following, we will compute both $G_{\mathrm{BV}}$ and $G_{\mathrm{SV}}$ with the same canonical scalar product $(\cdot,\cdot)$ and compare the results.

## III. FIXED POINTS, STABILITY, AND BIFURCATIONS

Within the physically acceptable range of parameters proposed by Charney and Devore, one wants to find a value of the forcing for which the model oscillates between two or more well-identified regimes. The two stable fixed points found by Charney and Devore for the three-dimensional (3D) model correspond roughly to blocked and zonal flows in the midlatitudes of the northern hemisphere; see Chap. 6 of Ghil and Childress[23] or Ghil and Robertson[24] for a review of this issue.

In the six-dimensional (6D) model, Charney and Devore found that one of these two fixed points lost its stability and oscillatory solutions were possible; see also Ref. 84. Legras and Ghil[41] showed that it was the blocked flow in their 25-component model on the sphere that underwent a Hopf bifurcation, as confirmed also in a rotating-annulus experiment.[77,82]

Following the conjecture of Charney and Devore and Ref. 41 that the regimes are associated with the presence of fixed points, we examine here the model's fixed points and their stability as a function of the forcing parameter $\psi_1^*$.

### A. Bifurcation diagram and stability analysis

The fixed points of the system of equations (3) have been studied extensively in Refs. 13, 17, 18, 23, and 84 among others. In the following, we refer to the full system of equations (3) as the "6D model," while the system truncated to the first three modes—$F_1$, $F_2$, and $F_3$—will be called the "3D model." The systematic comparison between the bifurcation diagrams of these two models that we provide below is, to the best of our knowledge, new and so is the connection we establish in the present section between these two bifurcation diagrams and the model dynamics, projected onto its leading EOFs.

As seen in Eq. (A6), the first three modes have maxima at midchannel and, following Lorenz,[45] are called of mode 1, while the next three modes have a neutral line at midchannel and are called of mode 2. The presence of the latter allows one to describe flow patterns with tilting ridges and troughs.

We compute first the fixed points of the 6D model for different values of $\psi_1^*$ using the AUTO software of Doedel *et al.*[20] The results are shown in Fig. 1.

Figure 1 provides two different views of the bifurcation diagram "fixed point versus parameter:" $\psi_1$ of the fixed point as a function of the forcing parameter $\psi_1^*$ (upper panel) and $\psi_4$ as a function of $\psi_1^*$ (lower panel). We follow the usual convention of indicating stable branches by solid lines and unstable ones by dashed lines. The letters associated with the subscripts $X_*, X_1, X_2, \ldots, X_6$ denote the coordinates of the point $X$ on the corresponding axes $\psi_1^*, \psi_1, \psi_2, \ldots, \psi_6$.

Steady solutions on the branch $OABCD$ correspond to the fixed points of the reduced, 3D model; cf. Fig. 6.5 of Ghil and Childress;[23] on this branch $\psi_4 \equiv \psi_5 \equiv \psi_6 \equiv 0$. These are the equilibria already studied in depth by Charney and Devore for $\psi_1^*=0.2$, although our choice of taking $\bar{\lambda}^2 \neq 0$ produces slightly different results. This branch remains the same for the 3D and the 6D model, but its stability differs: the branch $AB$ that was initially stable in the 3D model becomes unstable in the presence of perturbations in the three other mode-2 variables. This instability results in a supercritical Hopf bifurcation at point $A$, in agreement with Charney and Devore and Refs. 41 and 84. The limit cycle that arises from this Hopf bifurcation is very well described by the first two EOFs computed in Sec. III D below.

The branches $OA$ and $CD$ remain stable in the presence of mode-2 perturbations, and $A_* > C_*$. We conclude that, for all values of $\psi_1^*$, there exists at least one stable equilibrium: the branch $OA$ for small values of the forcing $\psi_1^*$ and the branch $CD$ for $\psi_1^* > 0.2$. The latter branch extends well outside the boundaries of Fig. 1 and asymptotes to the curve $\psi_1=\psi_1^*$, which corresponds to a zonal circulation; see again Sec. 6.3 in Ref. 23.

The branch $EFGH$ in the upper panel contains two distinct fixed points, $F$ and $F'$, as seen in the lower panel. The two solutions are symmetric with respect to the axis $\psi_4=0$, as well as with respect to the hyperplane $\psi_5=\psi_6=0$ (not

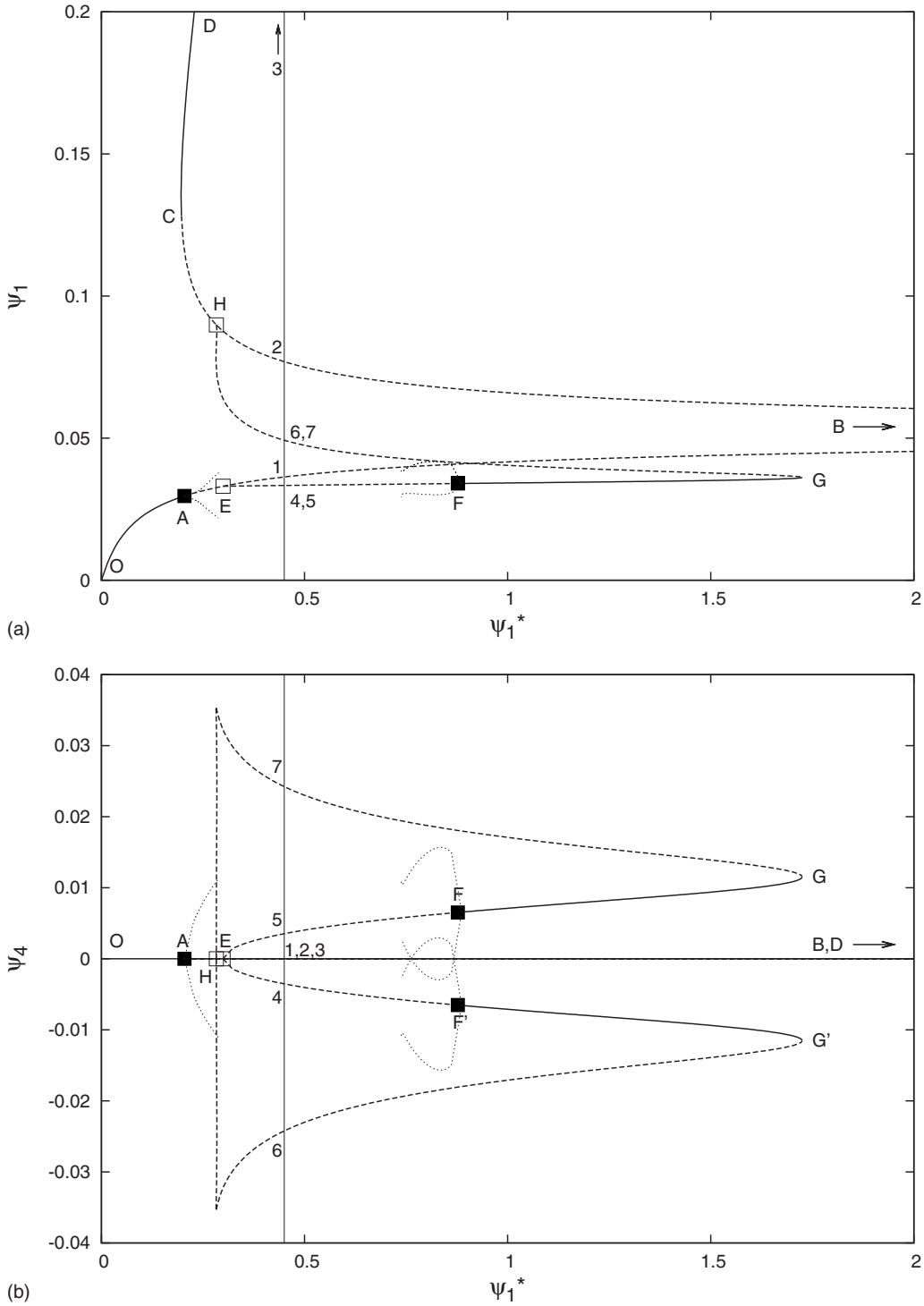


FIG. 1. Bifurcation diagram of the CDV model projected onto two coordinate systems: the upper panel shows the plot in the plane $(\psi_1^*, \psi_1)$ and the lower panel in the plane $(\psi_1^*, \psi_4)$; stable branch (solid) and unstable branch (dashed). Open squares denote branching points and filled squares denote Hopf bifurcations, while the letters mark points of interest on the curves, and numbers mark solutions for the parameter value $\psi_1^*=0.45$. The dotted lines mark the maxima and minima of the periodic orbit arising from the Hopf bifurcation at points $A$, $F$, and $F'$. This diagram expands and unifies the diagrams in Ref. 84.

shown). The two points $F$ and $F'$ correspond both to subcritical Hopf bifurcations: the branch $FG$ is stable for $F_* < \psi_1^* < G_*$, while the branch $GH$ is unstable.

When studying the dependence of the solutions on topographic height $h_0$ (not shown), we find that, in agreement with Charney and Devore, the shape of the bifurcation curves—shown in Fig. 1 for $h_0=0.1$ and channel width $L=r_0/4$—varies only slowly with $h_0$. As $h_0$ tends to zero, the range of coexistence of six unstable solutions diminishes and eventually only a single, stable solution remains. On the contrary, if we keep increasing $h_0$, the range of coexistence of multiple equilibria, albeit unstable ones, becomes larger.

As already mentioned by DeSwart,[17] the solutions of the 6D model are highly dependent on the channel width $L$. Still, our results do remain valid for a range of values of $L$ around the chosen value of $L=r_0/4$.

TABLE I. Algebraically largest and smallest real part of the eigenvalues of the Jacobian of Eq. (3) computed for all the fixed points at $\psi_1^*=0.45$. The imaginary part is indicated (in parentheses) for the complex-conjugate eigenvalues.

| Point | Max. eigenvalue | Min. eigenvalue |
|---|---|---|
| 1 | 0.048 | −0.066 |
| 2 | 0.097 | −0.095 |
| 3 | −0.005 | −0.009 ($\pm 0.623i$) |
| 4 and 5 | 0.006 ($\pm 0.034i$) | −0.031 |
| 6 and 7 | 0.076 | −0.075 |

The results of our stability analysis are summarized in Table I, which lists the eigenvalues of the Jacobian matrix corresponding to Eq. (3) for all the fixed points obtained at $\psi_1^*=0.45$ (see the vertical line in Fig. 1). Only the eigenvalues that correspond to the most stable and most unstable mode are given.

### B. Fixed points in physical space

Figure 2 illustrates the flow patterns of the fixed points in physical space for $\psi_1^*=0.45$; their numbering refers to that shown in Fig. 1, and all values are nondimensional.

As already stated, the first three fixed points have no mode-2 components, and thus all their ridges and troughs are purely meridional. As discussed by Charney and Devore (see their Fig. 4), the flow pattern in panel (1) is highly blocked, with its ridges very pronounced and way upstream of the topography, while the flow in panel (3) is almost purely zonal and its very small ridges are in phase with the topography; see also Refs. 23 and 24. The flow in panel (1) is fairly unrealistic, being a highly idealized version of a West Coast ridge, upstream of the Rockies.

Points 4 and 6, on the one side of the hyperplane $\psi_4=\psi_5=\psi_6=0$, and 5 and 7 on its other side have their mode-2 components pairwise symmetric with respect to this hyperplane (see lower panel of Fig. 1), while the zonal component $\psi_1$ differs from one member of each pair to the other (see the figure's upper panel). This partial symmetry is apparent in panels (4)–(7) of Fig. 2: the tilts of the ridges and troughs of panels (4) and (6) are opposite to those of panels (5) and (7), respectively, while the zonal flow is stronger in panels (6) and (7) than in (4) and (5).

### C. Model dynamics: Time-dependent solutions

Knowing the position and the stability of the fixed points for a wide range of values of the forcing $\psi_1^*$, we proceed to numerical integrations of the model for different values of $\psi_1^*$ and inquire whether there is an interaction between the fixed points and the model's dynamic behavior. The model is integrated using a predictor-corrector scheme with a time step of 0.01 nondimensional time units (about 2 min in dimensional time) in order to obtain a time series that is 1000 days long.

For $\psi_1^*<A_*$ and $\psi_1^*>G_*$, the trajectories converge toward the unique stable fixed point on the branch *OA* or *CD*, respectively. For other values of $\psi_1^*$, it is difficult to estimate—in the 6D model's phase space—the precise basin

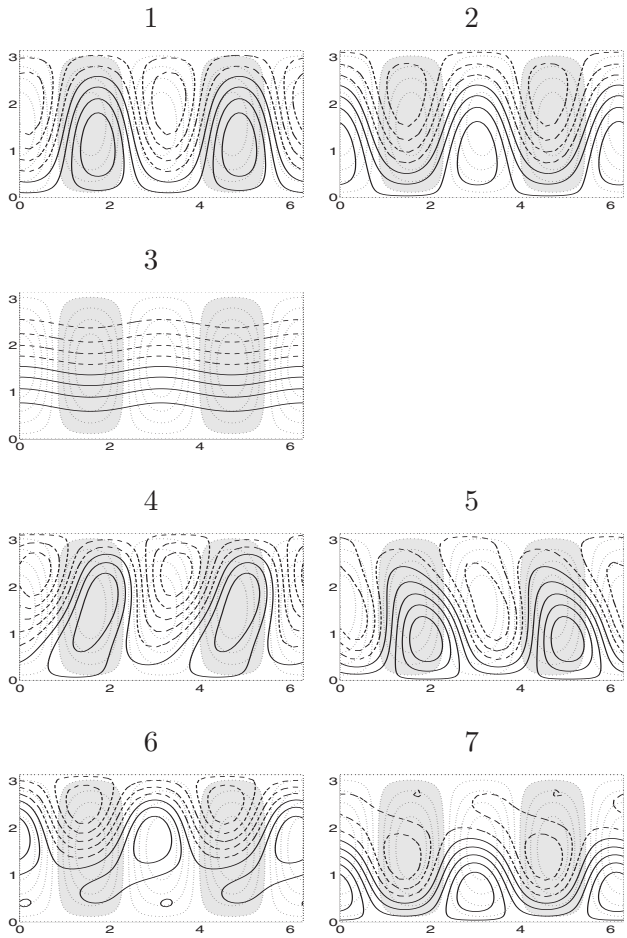


FIG. 2. The seven fixed points of the 6D model of CDV plotted in physical space for $\psi_1^*=0.45$; of the seven, panels (1)–(3) represent the fixed points of their 3D model. Black contours positive and dashed contours negative; the topographic ridges are shown as dotted contours (negative in gray).

of attraction of the fixed points on the two stable, coexisting branches *FG* and *CD*. Over a small range of $\psi_1^*$, though, included between the two Hopf bifurcations at $A_*$ and $F_*$, we observed that, for many initial states, the trajectories do not converge to the only stable fixed point, which corresponds to zonal flow (branch *CD*). For values of $\psi_1^*$ around 0.5 and for "good" initial states, the model behaves chaotically: the trajectories converge to an apparently strange attractor and we show below that, on this attractor, multiple regimes coexist.

From this preliminary numerical exploration, it follows that the 6D model exhibits at least two different types of behavior, with a unique, stable equilibrium or with more complex variability. We will study the model's behavior in greater detail for $0.4<\psi_1^*<0.5$ while using the set of parameter values given in Sec. II A.

### D. EOF analysis

We are looking for a subspace in which the model's multiple regimes, as well as its time-dependent behavior, appear as clearly as possible. For different values of $\psi_1^*$, we proceeded to an EOF analysis of the model output. The EOFs for $\psi_1^*=0.42$ were calculated from a 10 000-day-long time series, taking a sample pattern every 3 h; they are shown in Fig. 3. The EOFs for other $\psi_1^*$-values in the interval

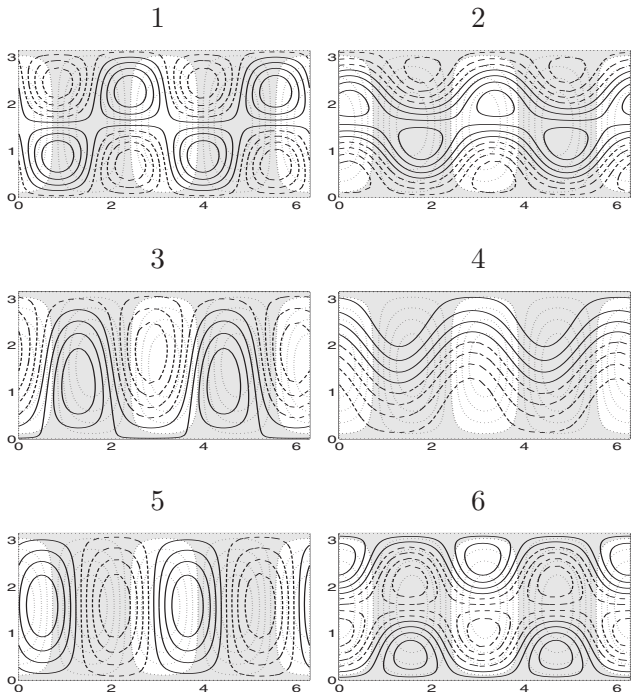


FIG. 3. EOFs of the 6D model for $\psi_1^*=0.42$. The associated variances are 49%, 17%, 14%, 11%, 6%, and 2%, respectively.

of interest are either individually similar to those shown in the figure or given (at least approximately) by some linear combinations of the latter; we present therefore all the results in the basis displayed in Fig. 3.

To compare the flow patterns of the fixed points with that of the EOFs, we subtract the overall mean of the long simulation, i.e., its climatology, from each of the fixed points (not shown). In climate dynamics, the difference between the actual pattern and the climatology is called the "anomaly." The fixed points 4 and 5 correspond to the positive and negative versions of EOF-1, respectively, while EOF-2 does not correspond to any fixed point. The flow pattern of EOF-3 is blocked and very similar to the anomaly of the first fixed point, while the zonal-flow dominated pattern of EOF-4 resembles the third fixed point. The second, unstable fixed point's anomaly has some similarity with EOF-5.

EOF-1 captures almost half the variance of the model behavior and is clearly associated with its alternating between the flow patterns of points 4 and 5, as we shall see also in Sec. III E. Inspection of panels (4) and (5) of Fig. 2 suggests that this dominant variability is associated with so-called tilted-trough vacillation,[31,64] a process that has been widely associated with the atmospheric index cycle.[45,61,69] More recently, an intraseasonal oscillation involving northern hemisphere topography has been shown to exhibit such a tilted-trough vacillation in both GCMs (Refs. 55 and 56) and atmospheric observations.[49,50]

### E. Dynamics in the subspace of the first two EOFs

A short section of the 6D model's trajectory, along with the position of the fixed points in the subspace spanned by the first two EOFs, is plotted in Fig. 4 for $\psi_1^*=0.45$. Several of the fixed points clearly affect the shape of the trajectory in the figure.

The large-scale flow pattern in the (EOF-1,EOF-2) plane is clockwise. The most stable and unstable directions of point 1 are associated with a negative and a positive real eigen-

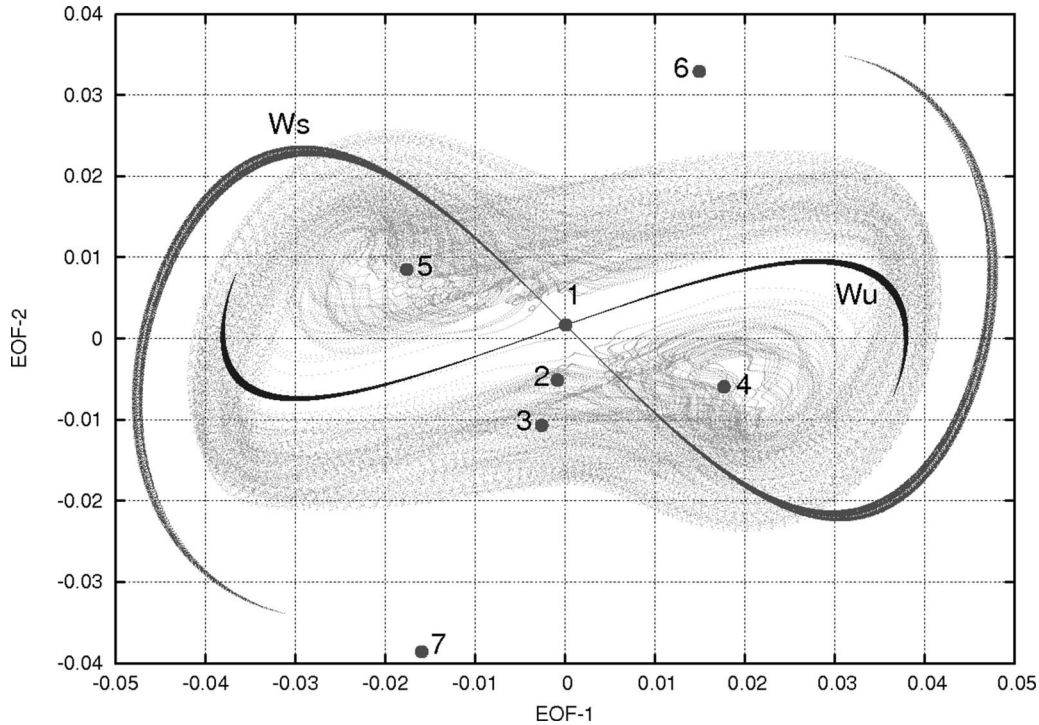


FIG. 4. Projection of the seven fixed points and projection of the stable and unstable manifolds of point 1, $W_s$ and $W_u$, on the plane of the first two EOFs. The segment of trajectory plotted is 9000 days long (about 300 oscillations); $W_s$ and $W_u$ were obtained here by backward and forward integrations, respectively, of model trajectories.

value (cf. Table I), respectively, and the phase-space flow near point 1 has a saddle-type behavior, with the trajectory running along the most unstable direction and away from the fixed point. On the contrary, the most unstable modes of points 4 and 5 are associated with a pair of complex-conjugate eigenvalues and induce a clockwise rotation around them.

The global evolution of the trajectory thus represents a superposition of the large-scale oscillation around these three points and of smaller-scale oscillations around point 4 or 5. We notice, therewith, a certain similarity with the role of the conductive saddle and the convective foci in the Lorenz[44] model or the saddle and foci in the nonlinear pendulum; please see Appendixes B and C. The other fixed points seem to have less of an influence on the trajectory.

The three possible regimes in our 6D CDV model are thus the "tight" oscillation around point 4, the tight oscillation around point 5, and the "wide" oscillation around all three points. The typical duration of a tight oscillation is about 20 days, a value that matches well the period associated with the imaginary part of the eigenvalue in Table I, which is 21 days.

We can now justify the choice of the range of values taken for $\psi_1^*$: for $\psi_1^*<0.4$, the model only produces the wide oscillation, while for $\psi_1^*>0.5$, the tight oscillations occur almost exclusively. The forcing level $\psi_1^*=0.45$ is thus a good intermediate value to study regime transitions.

## IV. PREDICTABILITY AND THE STABLE MANIFOLD

In this section, we study the predictability properties of the 6D model in the multiple-regime range of $0.4<\psi_1^*<0.5$. We will rely on the concepts of stable and unstable manifold in order to characterize the predictability in different regions of the phase space and will compare the results so obtained with those obtained from an application of the measures of local predictability described in Sec. II B.

### A. The stable and unstable manifolds

Stable and unstable manifolds are useful tools in studying the asymptotic behavior of geophysical dynamical systems (e.g., Refs. 23, 36, 47, and 81), as well as of turbulent two-dimensional (2D) flows (e.g., Ref. 29). In this work we extend their use to the present system, whose Kaplan–Yorke dimension[27] equals 3.25.

In the following, the results will be projected on the plane spanned by the first two EOFs, as in Fig. 4. In this subspace we can establish an analogy with a 2D flow containing a saddle point and two homoclinic orbits.

A stable and an unstable manifold, $\mathcal{W}_s$ and $\mathcal{W}_u$, respectively, can be associated with the saddle point near the model's climatological mean (point 1 in Fig. 4). The phase-space flow converges toward this saddle point, forward and backward in time, along $\mathcal{W}_s$ and $\mathcal{W}_u$, respectively. Indeed a particle lying near $\mathcal{W}_s$ will approach the saddle along that manifold and move away from it along $\mathcal{W}_u$.

Furthermore, pairs of particles, initially straddling $\mathcal{W}_s$, separate along either branch of $\mathcal{W}_u$. In other words, initial states in the neighborhood of $\mathcal{W}_s$ can follow either one of the branches of $\mathcal{W}_u$ or the other and then visit different regions of the phase space. When these regions correspond to distinct regimes of the model's behavior, the saddle will steer the flow to one or the other of these regimes. It is thus convenient to use the stable and unstable manifolds to define qualitatively distinct flow domains and to characterize exchanges between such domains. Figure 5 is based on the analysis of the Hamiltonian model studied in Appendix B and displays a schematic diagram of this situation.

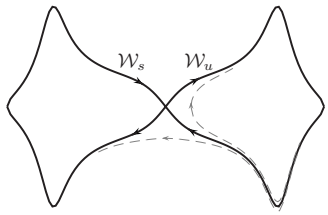


FIG. 5. Illustration of two homoclinic orbits joined at a saddle point. The stable and unstable manifolds of this point are denoted by $\mathcal{W}_s$ and $\mathcal{W}_u$. The dashed lines represent the evolution of two initial states that lie on either side of $\mathcal{W}_s$ and subsequently separate along the two branches of $\mathcal{W}_u$. This figure is based on the more intuitive Hamiltonian system introduced in Appendix B.

In our case, this intuitive idea of separation agrees quantitatively with the fact that the dimension $n_s$ of $\mathcal{W}_s$ equals 5 and the dimension $n_u$ of $\mathcal{W}_u$ is unity. As pointed out in Sec. 6.4 of Ghil and Childress[23] (see, in particular, Fig. 6.12 there), it is typically the case that $0<n_u\ll n_s$, while the set on which $n_u+n_s<n$, where $n$ is the total dimension of the problem's phase space, is the *bifurcation set*; this set has measure zero in the problem's phase-parameter space (see Fig. 1 here). In full GCMs, $n_s$ is large because of the presence of dissipation operators associated with or related to the Laplacian—an operator whose eigenvalues are negative and tend to $-\infty$—while $n_u$ is still relatively small (e.g., Ref. 6) and associated with well-defined physical instabilities, barotropic, baroclinic, or convective.

Haller[29] presented a particularly interesting method for computing the stable manifold, based on the *finite-map* technique introduced by Bowman.[4] The method is based on a formula that approximates the stable manifold $\mathcal{W}_s$ in a 2D flow by the local maxima of the function

$$S_T(x_0)=\max_{y\in G_{x_0}}\frac{\|x(T,y)-x(T,x_0)\|}{\|y-x_0\|}, \tag{12}$$

where $x(t,x_0)$ denotes a solution over the time interval $t\in[t_0,t_0+T]$ with initial condition $x_0$, and $G_{x_0}$ denotes the set of nearest neighbors of the point $x_0$. A good choice of $T$ is needed to find the manifold.

This equation was introduced in the context of 2D flows, and its validity has not been rigorously proven in higher-dimensional systems. Still, we will use here the growth rate of the BVs and SVs, introduced in Sec. II, as two practical approximations of the right-hand side of Eq. (12). In fact, $G_{\mathrm{BV}}$, $G_{\mathrm{SV}}$, and $S_T$ are all three estimators of the maximum growth rate over a given time interval $T$ at phase-space location $x$. If the local maxima of $S_T$ do indeed approximate $W_s$, as shown in Ref. 29 in the 2D case, then one can expect the local maxima of $G_{\mathrm{BV}}$ and $G_{\mathrm{SV}}$ to approximate $W_s$ as well.

Since $G_{BV}$ and $G_{SV}$ are easier to compute than $S_T$, such a result would be quite helpful. The stable manifolds found by computing $G_{BV}$ and $G_{SV}$, respectively, will be compared with the stable manifold of point 1 in the CDV model; cf. Figs. 4 and 5.

It is well known from the rich literature on BVs and SVs that the time interval $T$ over which these vectors are calculated has a very noticeable effect on the results; see again Refs. 78 and 79 and Ref. 5, respectively, as well as many subsequent references. The choice of $T$ in operational weather forecasting is mostly based on a trade-off between dynamical considerations and computer time constraints.

Full-blown, high-resolution numerical weather prediction models contain atmospheric waves with several characteristic times: the fastest are the gravity modes, next are baroclinic eddies (the storm systems of the midlatitudes), and slowest are the barotropic modes explicitly resolved by the CDV model. The choice for the breeding time of BVs, as well as of optimization of SVs, is nowadays of $T \simeq 2$ days, which corresponds roughly to the time needed for the most rapid gravity modes to saturate and allows one to concentrate on the error growth due to the baroclinic eddies.

We are looking instead for an optimal time $T$ over which the most rapid growth of the BVs and SVs is located near the stable manifold of fixed point 1. This value of $T$ is associated, as we shall see, with the system's predictability time.

### B. Results

First of all, we compute the stable and unstable manifolds of the saddle point of the CDV model. These are represented in Fig. 4. The unstable manifold is obtained by integrating the model from an ensemble of initial points located near point 1. The stable manifold is obtained from a similar initial ensemble but by integrating the model backward in time.

In Fig. 6, the local growth rates ($G_{SV}$ and $G_{BV}$) are shown as computed at different locations of the phase space. Fastest growth is indicated by warm colors and slowest by cool ones.

For small $T$, the zones where $G_{SV}$ takes its maximal values [red in panels (b) and (d)] are quite distinct from the zones where $G_{BV}$ is maximal [red in panels (a) and (c)]. The SV approach clearly exhibits two zones of very low predictability in the top-right and lower-left corners, while the BV growth rates are largest closer to where the projection onto EOF-1 is zero. None of these zones corresponds to the stable manifold of Fig. 4.

For higher values of $T$, between 5 and 12 days, the growth rates $G_{BV}$ and $G_{SV}$ take their respective maximal values over a fairly similar area; see panels (e)–(h) of Fig. 6. Comparing with Fig. 4, there is good agreement between this area and the stable manifold, especially close to the fixed point; the agreement extends further out at $T=11.2$ days.

The BV and SV growth rates computed in the red zones of panels (a)–(d) are high because they correspond to trajectory segments that diverge from one another while remaining within the "wide-oscillation" region. Conversely, the vectors that exhibit high growth rates in panels (e)–(h) correspond to zones where the trajectories can either stay on the wide oscillation around point 1 or begin a "tight oscillation" around point 4 or point 5. These are the zones where the trajectories separate in order to choose between one oscillatory regime and the other one. The rapid-divergence zones of panels (a)–(d) do not lead to immediate regime transitions. Their high growth rate is due to a higher local phase speed.

This difference in growth rate behavior for long and short optimization times will be verified in Sec. V. The issues of error growth via regime transition versus the better-understood uniform divergence of trajectories will be further discussed in Sec. VI.

Further increasing the renormalization time $T$ yields a uniform distribution of $G_{SV}$ over the attractor (not shown). This is in agreement with Goldhirsch *et al.*,[26] who proved that the first singular value of the normal operator in Sec. II B 2 converges to the leading Lyapunov exponent $\Lambda_0$ of the system for high $T$. We verified that the value of $G_{SV}$ in this limit equals $9.97 \times 10^{-7}$ s$^{-1}$, which is indeed the value of the model's first Lyapunov exponent. The same convergence toward $\Lambda_0$, as $T \to \infty$, was found for $G_{BV}$, although no theoretical result is available so far in this case.

Similar numerical experiments were carried out using finite-size Lyapunov exponents (cf. Aurell *et al.*[1] and Joseph and Legras[36]) and very similar results were obtained (not shown). Our results of Fig. 6 are also robust with respect to reasonable changes in the forcing $\psi_1^*$.

The optimal choice of renormalization time $T^*$ needed to find the stable manifold [cf. Eq. (12)] and to detect the zones of low predictability for regime transition (cf. Fig. 6) is of the same order of magnitude in our 6D model as the inverse of the leading Lyapunov exponent, $\Lambda_0^{-1}$. The same approximate equality seems to hold for other low-order dynamical systems (see Appendixes B and C).

We propose this value of $T^*$ as a lower bound on predictability time: in fact if two initial points are located near $\mathcal{W}_s$, $T^*$ is the time needed to observe a clear separation of the two trajectories. If the initials points are situated elsewhere, the time needed to observe the separation of the trajectories will be the same or higher.

## V. ENSEMBLE FORECASTS AND REGIME PREDICTABILITY

### A. Methodology

Legras and Ghil[41] first found a difference between the usual predictability limit—associated with uniform divergence of trajectories and characterized by the leading Lyapunov exponent, $\Lambda_0^{-1}$—on the one hand and regime predictability—which they associated with residence time in a regime and transitions between regimes—on the other; see also Sec. 6.4 of Ghil and Childress.[23] In this section, we verify that high values of $G_{BV}$ and $G_{SV}$ at different renormalization times $T$ do correspond to different types of divergence of the system's trajectories, and hence to different predictability properties. The verification is done by observing the time evolution of an ensemble of trajectories in the 6D model's phase space, initialized in areas of high $G_{SV}$ and $G_{BV}$ values.

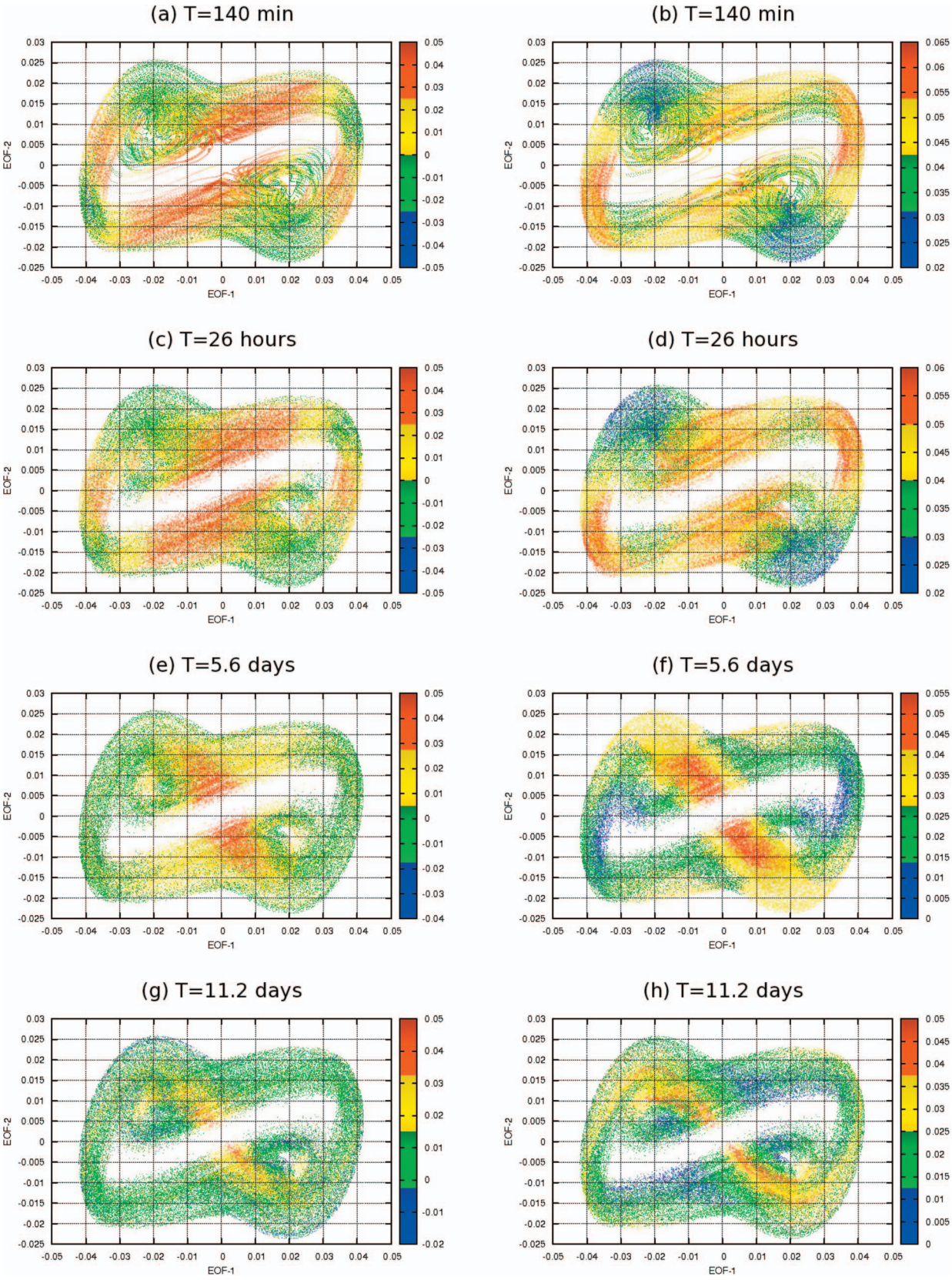


FIG. 6. (Color) Snapshot of $10^5$ points on the same trajectory taken every renormalization time $T$. The color measures the growth rates $G_{\mathrm{BV}}$ (left column) and $G_{\mathrm{SV}}$ (right column) for different values of $T$ (indicated above each panel). Zones of low predictability are associated with high values of $G_{\mathrm{BV}}$ (or $G_{\mathrm{SV}}$); these zones change with $T$.

We consider 2000 points belonging to one trajectory. They are decorrelated in the sense that they are more than $T^*$ apart on the trajectory. The nondimensional coordinates of each point in the (EOF-1,EOF-2) plane are written as $(x_1,x_2)$. Considering the results of Sec. IV, we focus on three distinct zones of the phase space:

- Zone 1: high values of $G_{\mathrm{BV}}$ for short $T$, $Z_2=\{(x_1,x_2):0<x_1<0.02$ and $0.05<x_2<0.015\}$.
- Zone 2: high values of $G_{\mathrm{SV}}$ for short renormalization times $T$, $Z_1=\{(x_1,x_2):x_1>0.03$ and $x_2>0.005\}$.
- Zone 3: high values of $G_{\mathrm{BV}}$ and $G_{\mathrm{SV}}$ for longer, near-optimal $T$, $Z_3=\{-0.01<x_1<0$ and $0.005<x_2<0.015\}$.

These are roughly the characteristic zones of the attractor for which either the SV or the BV approach or both approaches give us a very low predictability.

In Figs. 7 and 8 the evolution of trajectories that originate from zones 1 and 3, respectively, at time $t=0$ is shown at times $t^*=1$, 5, 9, and 13 days. The results for zone 2 are qualitatively the same as for zone 1 (not shown).

The left columns of either figure show the probability distribution function of the points observed at time $t^*$ on trajectories that started at initial time $t=0$ from points in zone 1 or 3, as defined above. The PDFs in the left column are represented by the light solid contours, while the phase portrait of the attractor is repeated in gray in the background.

The two figures display two very different types of behaviors. The evolution of zone 1 has a much smaller spread, except at $t=1$ day [panel (a)]. In the following days, the spread is consistently higher for zone 3; bimodality for zone 3 appears already at day 5 [panel (c)] and the smaller PDF separates completely from the larger one by day 9 [panel (d)], while for zone 1 moderate multimodality arises only by day 13 [panel (g)]. The evolution of zone 1 (Fig. 7) remains at all times, except at the very end, within the wide-oscillation regime. Conversely, the bimodality of the evolution of zone 3 corresponds to one PDF maximum in the wide-oscillation regime and another one in the tight-oscillation regime, turning around point 4.

In the right column of Figs. 7 and 8, the evolution of the system is illustrated making use of a predictability-and-persistence measure introduced by Lorenz,[46] and further developed by Trevisan.[80] The idea underlying this measure harks back, actually, to a weather forecasting approach that predates the beginnings of numerical prediction, namely, the use of so-called analogs: given today's weather map, on day $t_1$, one searches in a catalog of past maps for a similar one. In the 1960s, the "data mining" for the same map was carried out simply in the memory of an experienced meteorologist from the operational center, and the map at time $t_0$, say, was found on a shelf in a traditional archive. The forecast from $t_1$ to $t_1+t^*$ was then issued based on the recorded evolution of the weather at the previous time, from $t_0$ to $t_0+t^*$.

Lorenz[46] modified this operational procedure to study how two very close states, i.e., a pair of analogs, evolve away from each other. For this purpose, he used the 5 years of northern hemisphere, twice-daily weather maps available at that time to compute the likelihood of finding truly close analogs in the data. This question is closely related to

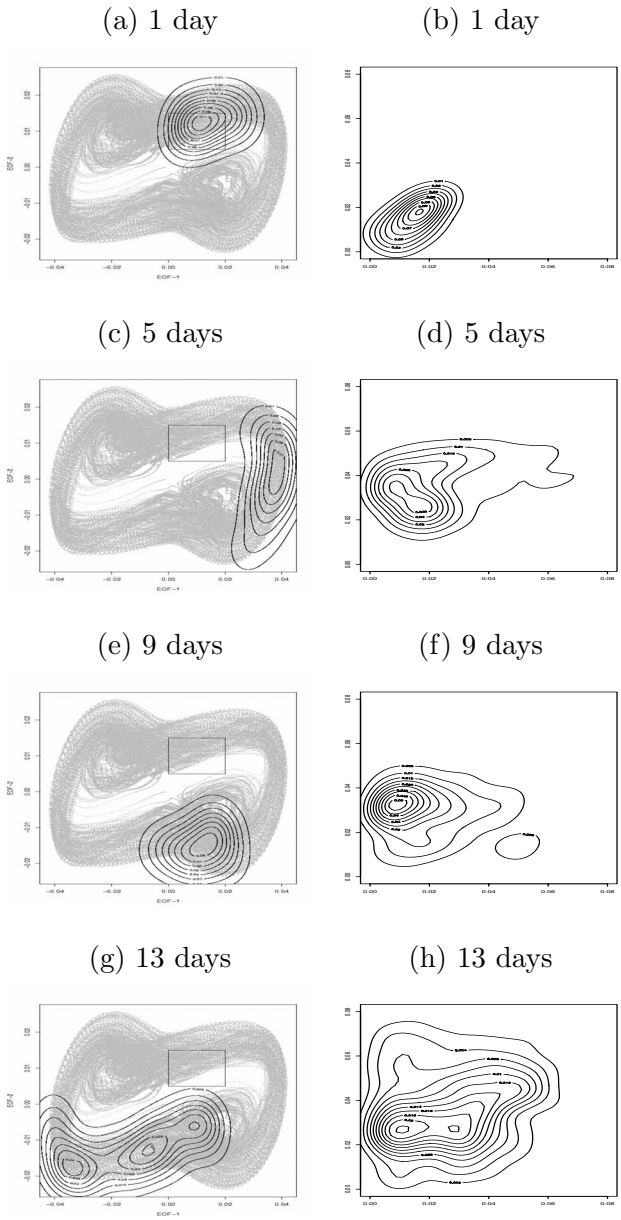


FIG. 7. Left column: Evolution of trajectories emanating from zone 1 at different target times $t^*$; zone 1 corresponds to high values of $G_{\mathrm{BV}}$ for short renormalization times $T$, and it is bounded by a rectangle in light solid. Right column: Bivariate PDF of $d_{\mathrm{pers}}$ vs $d_{\mathrm{pred}}$ at different instants $t^*$ of the evolution of the analogs; the PDF represents the number of analogs with values of $d_{\mathrm{pred}}$ on the abscissa and values of $d_{\mathrm{pers}}$ on the ordinate. See text for details.

Poincaré recurrence[2] and to the dimensionality of large-scale, midlatitude atmospheric flows. Other methods for determining this dimensionality are discussed in Sec. 6.5 of Ghil and Childress,[23] and all yield an order-of-magnitude estimate of roughly 100–200.

The exact formulation of Lorenz's analog-based predictability measure is the following: let $x_i^0$ denote a state vector at time $t=t_0$ and $x_i^t$ its transformation via the system after a time $t^*=t-t_0$. The evolution over time can be observed, as originally used by Lorenz,[46] or simulated, as we shall use it here.

Let $d(x_i^t,x_j^{t'})$ be the distance between two states $x_i^t$ and $x_j^{t'}$. To evaluate the local predictability at a given time $t_0$ of

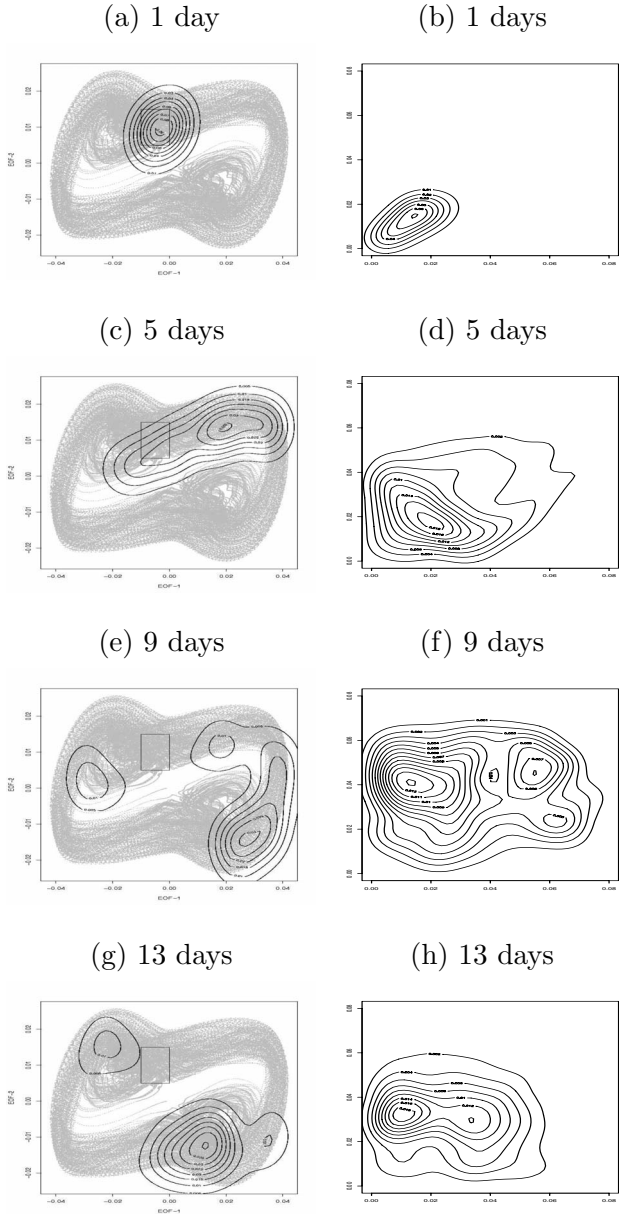


FIG. 8. Same as Fig. 7 but for zone 3; zone 3 corresponds to high values of $G_{BV}$ and $G_{SV}$ for near-optimal renormalization times $T$.

evolution over time $t-t_0$, we define the distance between the end points of the trajectories emanating from a pair of analogs $x_i^0$ and $x_j^0$ as $d_{pred}(t)=d(x_i^t,x_j^t)$. This distance tells us how far apart a pair of points that are initially close will separate and possibly be trapped in two different dynamic regimes after the time interval $t-t_0$.

To evaluate the persistence of the flow, we compute the evolution of the distance along a trajectory emanating from a given initial state $x_i^0$ using its analogs $x_j^0$ at the same time $t_0$: $d_{pers}(t)=d(x_i^t,x_j^0)$. We are thus estimating how far a trajectory departs from the neighborhood of its initial state.

All the distances between the points are Euclidean and computed in the reduced phase plane of (EOF-1,EOF-2), even though the BVs and SVs were computed in the 6D phase space. To select analogs, a distance threshold was chosen so as to have approximately the same number of analogs, namely, 30 000, in the three zones; the chosen threshold corresponds to a distance slightly smaller than the linear dimension of each zone. In the right column of Figs. 7 and 8, the predictability-persistence plots are shown at different evolution times $t^*=t-t_0$. Note that high predictability or persistence) corresponds to a small value of $d_{pred}(t)$ or $d_{pers}(t)$, respectively.

We find the same difference of behavior between points in zone 1 (Fig. 7) and in zone 3 (Fig. 8) as in the left column of the figures. For small values of $t^*$ [$t=1$ day, panel (e) of the two figures, or 2 days, not shown], the analogs do not have time to separate, either from each other or from their initial position, and the PDF is restricted to high persistence and high predictability. For large values of $t^*$ (more than 20 days, not shown), the PDF extends over the entire attractor.

At intermediate times, we observe marked differences in behavior between the two zones. At day 5 for zone 1, a shift along the persistence axis has occurred. This shift illustrates the high local phase-space speed, which displaces all analog pairs along the wide-oscillation region, and little change in the PDF occurs until day 9 [Fig. 7(f)].

The evolution from zone 3 has already a larger spread at day 5 and becomes multimodal by day 9 [see panels (f) and (h) of Fig. 8]. Dominant bimodality arises from the fact that some of the analog pairs are separated into two distinct regimes—wide oscillation and tight oscillation [see panels (e) and (f)] or tight oscillations around points 4 and 5, respectively, panels (g) and (h)—while other pairs stay in the same region of the attractor. Similar results are obtained using different thresholds of maximal initial distance for the analogs.

## VI. CONCLUDING REMARKS

The purpose of the present paper was to study key aspects of atmospheric LFV, in particular, the effect of multiple regimes on the flow's conditional predictability. More precisely, we wanted to investigate how local predictability may depend on the position and stability of the system's fixed points and their invariant manifolds. In addition, we wished to evaluate the contribution of methods currently in use in operational weather prediction to answering the paper's key questions.

### A. Summary

To provide some insight into these matters, we used the classical, 6D CDV model of Charney and Devore[8] in a parameter range in which it exhibits multiple regimes. These regimes are not simply bistable equilibria, as in the better-known 3D version of the CDV model, but exhibit different types of time-dependent behavior, as in Ref. 41. The two model versions share three mode-1 components—$\psi_1$, $\psi_2$, and $\psi_3$ [cf. Eqs. (A6) and (3)]—and differ by the presence of three mode-2 components, $\psi_4$, $\psi_5$, and $\psi_6$, in the 6D version.

We explored the 6D model's full bifurcation diagram, varying the intensity $\psi_1^*$ of the forcing jet (Fig. 1), and focused on the parameter range $0.4<\psi_1^*<0.5$; within this range, the model's time-dependent behavior can be used as a

"metaphor" for the multiple time and space scales of extratropical atmospheric dynamics on the time scale of days to months.

The 6D model has seven fixed points (see again Fig. 1) both stable and unstable (see Table I), whose spatial patterns are shown in Fig. 2. The model's multiple regimes are largely determined by the interplay of three of these fixed points and of their stable and unstable manifolds (see Fig. 4). Two unstable foci, which we labeled points 4 and 5, are situated symmetrically with respect to the hyperplane $\psi_4 = \psi_5 = \psi_6 = 0$, and each can intermittently trap the orbit into relatively "tight" oscillations around that point. These two oscillations, or "swirls," are reminiscent of those associated with the two convective points in the Lorenz[44] model and represent two of our 6D model's three regimes.

The model's overall chaotic phase-space flow switches irregularly between these two tight-oscillation regimes and a "wide-oscillation" regime that encompasses the two unstable foci, points 4 and 5, and the mode-1 saddle near the model's overall mean or "climatology," which we labeled point 1 (see again Fig. 4). The stable and unstable manifolds issuing from this saddle point, $\mathcal{W}_s$ and $\mathcal{W}_u$, were computed by backward and forward integrations, respectively, of the model equations (3) from suitable initial data (see Fig. 4). These manifolds appear to influence decisively the model's global dynamics: $\mathcal{W}_u$ separates the upper (positive projection on EOF-2, upper half-plane in Fig. 4) from the lower (opposite half-plane in the figure) half of the wide oscillation, while $\mathcal{W}_s$ separates the two tight swirls around points 4 and 5 from each other.

A key point of the present paper was to evaluate how local measures of predictability—currently in use in operational centers of weather prediction—can help approximate the stable manifold $\mathcal{W}_s$ of our model's central saddle point, since $\mathcal{W}_s$ clearly plays a guiding role in separating the regimes and affects the predictability of transitions between them. The two leading measures of this type are BVs (Toth and Kalnay[78,79]) and SVs (Buizza and Palmer[5]).

Using a formula due to Haller,[29] namely, Eq. (12), we were able to compute quite accurately the stable manifold $\mathcal{W}_s$. In fact, the growth rates $G_{\mathrm{BV}}$ and $G_{\mathrm{SV}}$—associated with the BV and SV approaches, respectively—provide relatively simple approximations to the right-hand side of Haller's formula.

For short renormalization times $T$, we found high values of $G_{\mathrm{BV}}$ and $G_{\mathrm{SV}}$ to be associated with zones on the attractor that are distinct from each other and both lying far from the stable manifold (see Fig. 6). For suitably chosen $T$, though, both the BV and the SV approach can help identify the correct stable manifold $\mathcal{W}_s$ of our model's near-climatological point 1. The appropriate value, at least for the 6D CDV model, is $T$ between 6 and 12 days (see again Fig. 6). We return to the interpretation of these results in Sec. VI B.

### B. Discussion

Legras and Ghil[41]—using a 25-component model on the sphere rather than in a $\beta$-channel, as used by Charney and Devore[8] or Lorenz[45]—showed that, in the presence of multiple regimes, one has to distinguish between the more-or-less uniform "pointwise predictability" of typical, Lyapunov-exponent based studies and what they termed "regime predictability." First of all, we confirmed that both $G_{\mathrm{BV}}$ and $G_{\mathrm{SV}}$ tend to the leading Lyapunov exponent $\Lambda_0$ as $T \to \infty$.

In Sec. V, we found that high values of the growth rates $G_{\mathrm{BV}}$ and $G_{\mathrm{SV}}$ do indeed correspond to two different types of divergence of the system's trajectories, and hence to different predictability properties. The difference between Figs. 7 and 8 is quite telling: at small renormalization times $T$, high $G_{\mathrm{BV}}$ is associated with phase separation along trajectories that stay within the wide-oscillation regime, while for near-optimal $T$, both high $G_{\mathrm{BV}}$ and high $G_{\mathrm{SV}}$ indicate trajectories that separate to join either one or the other of the swirls; the results for short $T$ and high $G_{\mathrm{SV}}$ are quite similar to those for short $T$ and high $G_{\mathrm{BV}}$.

Research studies centered around either the BV or the SV approach have emphasized the importance of optimizing the renormalization times $T$ for the growth of the BVs or SVs, respectively. Thus, Peña and Kalnay[63] studied a model coupling two Lorenz[44] systems, one slow and the other fast. They showed using BVs that a good choice of the renormalization time is of paramount importance in separating the slow from the fast dynamics, and thus obtaining the proper leading BV for the slow dynamics. Cai *et al.*[7] implemented similar ideas in a BV-based predictability study for an "intermediate" model of the ENSO the Zebiak and Cane[85] model.

Buizza and Plamer[5] likewise emphasized the need for properly choosing the time over which the SVs are optimized; cf. Eq. (11); for the sake of brevity, we call this time also "renormalization time," although the technical details are somewhat different in the two approaches. Here too, Xue *et al.*[83] obtained a certain degree of robustness of the SVs in applying them to Zebiak and Cane's ENSO model.

These and similar studies were mainly motivated by operational needs to compute a good initial cloud of points for ensemble forecasts or directions of optimal updates in data assimilation. The choice of the renormalization time $T$ in operational weather forecasting is mostly based on trade-offs between dynamical and practical considerations. These considerations include, but are not limited to, numerical constraints (either algorithmic or involving the availability and distribution of computer power), the length of the assimilation cycle (in the case of BVs), or the need of satisfying the linear approximation to a satisfactory degree (in the case of SVs). *A posteriori*, an optimal renormalization time of a couple of days is often justified by baroclinic instability's being the main source of forecast error growth at the range of a few days of lead time.

In the present paper, we have added an interesting consideration to the ones already in use in meteorology. We have shown by using ensemble forecasts, as well as the BV and SV approaches, that short renormalization times tend to select directions of high divergence within the same regime, while longer renormalization times capture trajectory divergence due to regime transitions (see again Figs. 7 and 8).

These results show the importance of a good, and possibly longer, choice of renormalization time when using BVs or SVs in a regime-based predictability problem. Multiple

regimes are pervasive in many nonlinear problems Lorenz,[48] not only in meteorology, oceanography, and coupled ocean-atmosphere climate dynamics but also in the geosciences in general, as well as in ecology and the life sciences. To the extent that prediction at both short and longer lead times is an issue, the results reported here might present some interest in these broader contexts. In many nonlinear problems—independently of their origin—short-range prediction corresponds to "beating" rapid error growth within the same regime, while longer-range prediction requires identifying and foretelling regime transitions.

Due to the simplicity of the CDV model, the present study is highly idealized and applying its results to the real, infinite-dimensional atmosphere or ocean can only proceed via the by now well-trodden path of pursuing these results through a full hierarchy of models, as outlined by Schneider and Dickinson,[71] Ghil and Robertson,[25] and Ghil.[22] In this approach, ideas developed in highly simplified, so-called toy models with but a few or just a few tens of degrees of freedom have to be further tested in intermediate models, with hundreds or thousands of degrees of freedom and greater physical realism, such as the Zebiak and Cane[85] model, and finally in full-blown GCMs, with millions of discrete variables.

## ACKNOWLEDGMENTS

It is a pleasure to thank S. Corti, E. Kalnay, B. Legras, C. Rousset, and A. Trevisan for discussions and suggestions. Two anonymous reviewers carefully read the paper and provided insightful and constructive comments. This work was supported by DOE Grant No. DE-FG02-07ER64439 from the Climate Change Prediction Program.

## APPENDIX A: FULL MODEL DESCRIPTION

The model is governed by the quasigeostrophic equation of potential vorticity for a fluid evolving in a rectangular channel of dimension $2\pi L \times \pi L$. This channel is located on a $\beta$-plane (e.g., Ref. 23) and has a free surface of height $H+\eta$:

$$\partial_t\left(\nabla^2\psi - \frac{\psi}{\lambda^2}\right) + J\left(\psi, \nabla^2\psi - \frac{\psi}{\lambda^2} + f_0\frac{h}{H} + \beta y\right) = -\frac{f_0 D_E}{2H}\nabla^2(\psi - \psi^*), \tag{A1}$$

where the Jacobian $J$ is defined as $J(A,B)=(\partial_x A\partial_y B - \partial_x B\partial_y A)$ and $\nabla^2$ is the Laplacian operator. All the variables, parameters, and constants are defined in Table II.

As usual, we nondimensionalize $t$ by $f_0^{-1}$, $x$ and $y$ by $L$, $\psi$ and $\psi^*$ by $L^2 f_0$, and $h$ by $H$. The equation in the new nondimensional variables is

TABLE II. Variables, parameters, and constants used in the CDV model.

| Parameter | Meaning | Value |
|---|---|---|
| $r_0$ | Radius of the earth | 6400 km |
| $L$ | $=r_0/4$ length scale | 1600 km |
| $\phi_0$ | Central latitude | 45° |
| $\Omega$ | Angular speed of the earth | $7.2\times10^{-5}$ rad $s^{-1}$ |
| $f_0$ | $=2\Omega \sin\phi_0$ Coriolis parameter | $1.028\times10^{-4}$ $s^{-1}$ |
| $\beta$ | $=(2\Omega/r_0)\sin\phi_0$ $\beta$-effect parameter | $1.6\times10^{-11}$ $m^{-1}$ $s^{-1}$ |
| $H$ | Mean height of the fluid | $10^4$ m |
| $g$ | Gravity constant | 3.6 m $s^{-1}$ |
| $\lambda$ | $=\sqrt{gH}/f_0$ deformation radius | $1.5\times10^6$ $m^2$ |
| $D_E$ | Ekman layer depth | 200 m |
| $h$ | Topographic height | |
| $\eta$ | Free-surface anomaly | |
| $\psi$ | $=g\eta/f_0$ | |
| $\psi^*$ | External forcing | |

$$\partial_t(\nabla^2\psi - \bar{\lambda}^2\,.\,\psi) + J(\psi, \nabla^2\psi + h) + \bar{\beta}\partial_x\psi = -k\nabla^2(\psi - \psi^*), \tag{A2}$$

with $\bar{\lambda}^2=(f_0^2L^2)/(gH)$, $\bar{\beta}=(L/r_0)\cot(\phi_0)$, and $k=D_E/(2H)$.

Equation (A2) is expanded in the eigenfunctions $F_i$ of the Laplacian operator, $\nabla^2 F_i=-a_i^2F_i$. These functions are chosen so as to be orthonormal—i.e., for all $(i,j)$,

$$\langle F_i, F_j\rangle \equiv 1/(2\pi^2)\int_{x=0}^{2\pi}\int_{y=0}^{\pi} F_iF_j\,dx\,dy = \delta_{ij},$$

where $\delta_{ij}$ is the Kronecker symbol—and to satisfy $\partial_x F_i=0$ at the channel walls $y=0,\pi$.

The functions $F_i$ so defined have the following properties:

$$\partial_x F_i = \sum_{j=1}^{\infty} b_{ij}F_j \quad \text{with} \quad b_{ij}=\langle F_j, \partial_x F_i\rangle \tag{A3}$$

and

$$\langle F_j, F_k\rangle = \sum_{i=1}^{\infty} c_{ijk}F_i \quad \text{with} \quad c_{ijk}=\langle F_i, J(F_j,F_k)\rangle. \tag{A4}$$

The constants $c_{ijk}$ verify $c_{ijk}=-c_{ikj}$ and $c_{ijk}=c_{jki}=c_{kij}$. Hence, developing $\psi$, $\psi^*$, and $h$ with respect to these basis functions, $(\psi,\psi^*,h)=\Sigma_{i=1}^{\infty}(\psi_i,\psi_i^*,h_i)F_i$, Eq. (A2) becomes

$$(a_i^2+\bar{\lambda}^2)\dot{\psi}_i = \sum_{k>j}^{\infty} c_{ijk}((a_j^2-a_k^2)\psi_j\psi_k - h_j\psi_k + h_k\psi_j) + \bar{\beta}\sum_{j=1}^{\infty} b_{ji}\psi_j - ka_i^2(\psi_i-\psi_i^*). \tag{A5}$$

Following the original idea of Lorenz,[45] we retain only six modes in order to capture key properties of the flow governed by Eq. (A1) in a low-dimensional model. These six leading modes and the associated eigenvalues are

$$F_1 = \sqrt{2}\cos y, \quad a_1^2 = 1,$$

$$F_2 = 2\cos nx \sin y, \quad a_2^2 = n^2 + 1,$$

$$F_3 = 2\sin nx \sin y, \quad a_3^2 = n^2 + 1,$$

$$F_4 = \sqrt{2}\cos 2y, \quad a_4^2 = 4, \tag{A6}$$

$$F_5 = 2\cos nx \sin 2y, \quad a_5^2 = n^2 + 4,$$

$$F_6 = 2\sin nx \sin 2y, \quad a_6^2 = n^2 + 4.$$

The topographic profile chosen by CDV was based on the midlatitude topography of the northern hemisphere first introduced by Charney and Eliassen[9] into the study of the interaction of large-scale atmospheric flow with mountain ranges. The topography in this earlier, pioneering paper was dominated by zonal wavenumber 2, and so Charney and Devore restricted their study to second-mode topography only, i.e., $h=h_0F_2$. Furthermore, we study our 6D model considering only a zonal, west-east forcing, so that $\psi^* = \psi_1^* F_1$.

The nonzero coefficients $b_{ij}$ are $b_{23}=-b_{32}=b_{56}=-b_{65}=-n$, while the nonzero coefficients of the quadratic terms $c_{ijk}$ are

$$\frac{c_{321}}{5} = \frac{c_{651}}{4} = \frac{c_{462}}{8} = \frac{c_{543}}{8} = \frac{8n\sqrt{2}}{15\pi} \tag{A7}$$

and all the corresponding permutations of the triplet $(i,j,k)$. The final low-order model is given by

$$\begin{aligned}
\dot{\psi}_1 &= -k_{01}(\psi_1 - \psi_1^*) + h_{01}\psi_3, \\
\dot{\psi}_2 &= -k_{n1}\psi_2 - (\alpha_{n1}\psi_1 - \beta_{n1})\psi_3 - \delta_{n1}\psi_4\psi_6, \\
\dot{\psi}_3 &= -k_{n1}\psi_3 + (\alpha_{n1}\psi_1 - \beta_{n1})\psi_2 - h_{n1}\psi_1 + \delta_{n1}\psi_4\psi_5, \\
\dot{\psi}_4 &= -k_{02}\psi_4 + \epsilon_n(\psi_2\psi_6 - \psi_3\psi_5) + h_{02}\psi_6, \\
\dot{\psi}_5 &= -k_{n2}\psi_5 - (\alpha_{n2}\psi_1 - \beta_{n2})\psi_6 - \delta_{n2}\psi_4\psi_3, \\
\dot{\psi}_6 &= -k_{n2}\psi_6 + (\alpha_{n2}\psi_1 - \beta_{n2})\psi_5 - h_{n2}\psi_4 + \delta_{n2}\psi_4\psi_1,
\end{aligned} \tag{A8}$$

with the following symbols:

$$\begin{aligned}
\alpha_{n1} &= \frac{n^2}{n^2 + 1 + \bar{\lambda}^2} c_{321}, \\
\alpha_{n2} &= \frac{(n^2+3)}{n^2 + 4 + \bar{\lambda}^2} c_{651}, \\
\delta_{nm} &= \frac{(n^2 - m^2 + 1)}{n^2 + m^2 + \bar{\lambda}^2} c_{462}, \\
\epsilon_n &= \frac{3}{4 + \bar{\lambda}^2} c_{462}, \\
k_{nm} &= \frac{n^2 + m^2}{n^2 + m^2 + \bar{\lambda}^2} k, \\
h_{n1} &= \frac{c_{321}}{n^2 + 1 + \bar{\lambda}^2} h_0, \\
h_{n2} &= \frac{c_{462}}{n^2 + 4 + \bar{\lambda}^2} h_0, . \\
\beta_{nm} &= \frac{n}{n^2 + m^2 + \bar{\lambda}^2} \bar{\beta}.
\end{aligned} \tag{A9}$$

We study this model in the main text for the following fixed parameter values—$n=2$, $k=10^{-2}$, $\bar{\beta}=0.25$, and $h_0=0.1$—while $\psi_1^*$ is the bifurcation parameter. Unlike by Charney and Devore and as in Ref. 41, we keep a free upper surface by letting $\bar{\lambda}^2 \neq 0$.

## APPENDIX B: REGIME PREDICTABILITY FOR A HAMILTONIAN SYSTEM

In this appendix, we introduce a very simple Hamiltonian model. Its simplicity makes it more physically intuitive than the 6D model used in the main text; its multiple regimes can easily be visualized in a phase portrait, and it is possible to write the analytical expression of the stable manifold. We use it as a theoretical paradigm for the behavior of the CDV model. Note that Fig. 5 in the main text applies exactly to this model; see below.

The system has some similarity with the nonlinear elastic pendulum of Lynch.[51] While the elastic pendulum is just another formulation of the toy model of Lorenz,[47] our model here is better suited for multiple-regime studies; see also Lorenz.[48]

Our Hamiltonian toy model has two point masses connected by an elastic spring of rigidity $k$. The difference with respect to the classical nonlinear pendulum is that the two masses are constrained to evolve each along a prescribed curve (cf. Fig. 9). The first mass, $m_1$, evolves along a double-well curve given by equation $y=f_1(x)$; this curve has three equilibrium points, two stable and one unstable, and $m_1$ can oscillate around each of the stable points.

The second mass, $m_2$, evolves along a straight line $y=f_2(x)$, and it adds a perturbation to the motion of $m_1$. This

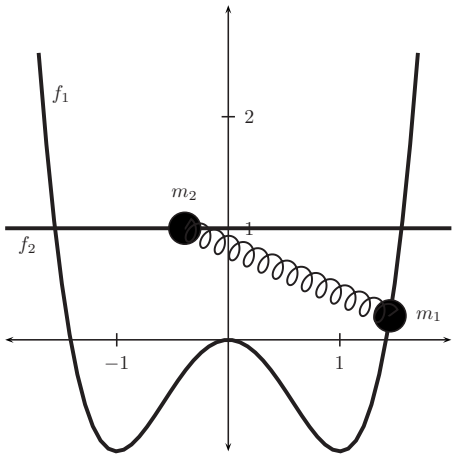


FIG. 9. Two point masses connected by an elastic spring: $m_1$ evolves along the double-well curve given by the equation $f_1(x)=x^4-2x^2$, while $m_2$ evolves on the straight line $f_2(x)=1$.

perturbation is small if either $m_2/m_1$ or $k$ are small; the smallness of the latter is determined by $k<m_1g/L$, with $L$ being a characteristic dimension of the problem that will be set to 1. In this case, the behavior of $m_1$ is very similar to the Duffing oscillator,[40] while $m_2$ behaves more like a simple, harmonic oscillator.

We choose the two curves as

$$f_1(x) = x^4 - 2x^2, \quad f_2(x) = 1. \tag{B1}$$

The parameters of our problem are the spring constant $k$ and the values $m_1$ and $m_2$ of the two masses. The oscillation frequency of $m_1$ is linked to the shape of the curve $y=f_1(x)$ and to the gravitational constant $g$, while the frequency of $m_2$ depends on the value of $k$. The three parameters can be adjusted in order to choose the frequency of each mass. For weak coupling, i.e., small $k$, $m_1$ will oscillate with high frequency, while $m_2$ will have a much slower motion.

### 1. Equation of motion of $m_1$ with no coupling ($k=0$)

Let $(x_1,y_1)$ be the position of the particle $m_1$ in the $(x,y)$ plane, with $x$ horizontal and $y$ vertical, while $(\dot{x}_1,\dot{y}_1)$ is its velocity. We are looking for the equation of motion of $m_1$ in the gravity field $(0,-g)$. Using the Lagrange multiplier $\lambda$, one has to minimize the constrained action integral

$$S = \int \left(\frac{1}{2}m_1(\dot{x}_1^2+\dot{y}_1^2) - m_1 g y_1\right)dt + \lambda \int (y_1 - f_1(x_1))dt. \tag{B2}$$

The resulting equations of motion are

$$\begin{aligned} m_1\ddot{x}_1 &= -\lambda f_1'(x_1), \\ m_1\ddot{y}_1 &= -m_1 g + \lambda, \end{aligned} \tag{B3}$$

subject to the constraint $y_1=f_1(x_1)$. Substituting the constraint into Eq. (B3) yields

$$\ddot{x}_1 = -\frac{\dot{x}_1^2 f_1'(x_1) f_1''(x_1) + g f_1'(x_1)}{1+f_1'(x_1)^2}. \tag{B4}$$

From this equation, we can construct a simple 2D dynamical system by introducing a new variable $u_1$ to yield $\dot{x}_1=u_1$ and $\dot{u}_1$ equal to the right-hand side of Eq. (B4). We note that the equilibria $(x_1^e,u_1^e)$ of the single particle $m_1$ are at $f_1'(x_1^e)=0$, where the acceleration is zero, i.e., at $x_1^e=\pm 1$ (stable) and $x_1^e=0$ (unstable).

### 2. The regimes of the single-mass oscillator

In such a simple system, a clear identification of the regimes is easy: one just has to apply the conservation of the energy,

$$\begin{aligned} E &= K + P, \\ K &= \tfrac{1}{2}m_1(u_1^2+\dot{y}_1^2), \\ P &= -m_1 g y_1, \end{aligned} \tag{B5}$$

to obtain

$$u_1^2 + \frac{2g(f(x_1)-f(x_1^0))}{1+f'(x_1)^2} = 0. \tag{B6}$$

Here $x_1(t=0)\equiv x_1^0$ is the initial condition for $x_1$ and we took $u_1^0=0$. This equation gives the contour of the trajectory $F(x_1,u_1;x_1^0)=0$ for a given energy level $E=E_0$ or, equivalently, a given initial state $(x_1^0,0)$.

We know that the closed orbits so described in a 2D, integrable system like that of (B4) represent purely periodic motions. The only exceptions are the homoclinic orbits shown in Fig. 5, in which the stable and unstable manifolds $\mathcal{W}_s$ and $\mathcal{W}_u$ are obtained by taking $x_1^0=0$ in Eq. (B6).

We plot the phase portrait $(x_1,u_1)$ for different values of $x_1^0$ (cf. Fig. 5) and see that we can define three regimes depending on the value of the initial condition: [(i) and (ii)] the mass $m_1$ can either oscillate periodically on one side only of the curve $y_1=f_1(x_1)$, i.e., in the half-plane $\{(x_1,u_1):x_1>0\}$ or $\{(x_1,u_1):x_1<0\}$, or it can (iii) oscillate across the symmetry line $x_1=0$, thus following a wide oscillation, as in the CDV model, if the initial value $x_1^0$ is large enough. The addition of the mass $m_2$ and the spring connecting the two will perturb the purely periodic motions of the particle $m_1$ described so far and will allow it to switch from one regime to another, as is the case in the 6D model of the main text.

### 3. The coupled-particle system

We now consider the case $k\neq 0$; the neutral length of the spring in the absence of any forces will be denoted by $l_0$. If we call $(x_2,y_2)$ the position of the second mass and $l=\sqrt{(x_2-x_1)^2+(y_2-y_1)^2}$ the distance between the two masses, the equations of motion for $m_1$ and $m_2$ are

$$\begin{aligned} \ddot{x}_1 &= -\frac{\dot{x}_1^2 f_1'(x_1) f_1''(x_1) + g f_1'(x_1)}{1+f_1'(x_1)^2} \\ &\quad + \frac{k(l-l_0)[(x_2-x_1)+f_1'(x_1)(y_2-y_1)]}{l m_1(1+f_1'(x_1)^2)}, \\ \ddot{x}_2 &= \frac{k}{l m_2}(l-l_0)(x_1-x_2). \end{aligned} \tag{B7}$$

The positions of the equilibria $(x_1^e, x_2^e)$ depend now on the value of $l_0$. For simplicity, we choose a configuration for which the equilibria are the same with and without the spring: they still have to satisfy $f_1'(x_1^e)=0$ in both cases, yielding $x_1^e=\pm 1$ and $x_1^e=0$, as before. Moreover, when we add the spring, its length $l$ has to verify $l=l_0$, and we take $l_0=2$ for our basic case. It follows from the geometry of the two constraints in Fig. 9 that $x_2^e=x_1^e=\pm 1$, and there is no equilibrium of the two-particle system with $x_1^e=0$.

For small values of $k$ ($k<mg/L$), the motion of $m_1$ is not substantially modified by the presence of $m_2$. Computing the leading Lyapunov exponent $\Lambda_0$ as a function of $k$, for given $m_2$, we find that $\Lambda_0$ increases linearly with $k$ (not shown).

In the following subsection, we choose $m_1=m_2$ and $k/m_1=0.2g/L$. This choice corresponds to chaotic behavior of the coupled system but still includes one of the smallest values of $k$ that permits regime transitions. Hence we assume that the three regimes defined in the preceding subsection do not change.

### 4. Regime predictability in the coupled system

We investigate now whether regime predictability is influenced by the central fixed point and, if so, whether this predictability is lowest near this point's stable manifold. Once again, we have several tools for our predictability study. We only show here the results obtained with the SV approach, but the results using BVs or local Lyapunov vectors are quite similar.

In Fig. 10, one can see that for small renormalization time $T$ (topmost panel), $G_{\mathrm{SV}}$ takes its highest values in those regions of the phase space where the particle $m_1$ has highest velocity. In fact for short-term prediction, the divergence of the trajectories near the stable manifold is much less than in these high-velocity zones. Moreover, the zones of high $G_{\mathrm{BV}}$ values (not shown) are located in other parts of the attractor. This property was already observed by Gyarmati *et al.*[28] for the elastic pendulum.

If we keep increasing $T$, the leading singular value of the normal operator defined in Sec. II B 2 converges to the first Lyapunov exponent, as verified already for the 6D model in the main text: the sensitive region of high $G_{\mathrm{SV}}$ values stretches and aligns along the analytically computed stable manifold (lowermost panel).

## APPENDIX C: APPLICATION TO THE LORENZ (REF. 44) MODEL

It would have been frustrating to complete this study without checking whether our results apply to the Lorenz[44] model as well. Evans *et al.*[21] already tried to predict the transitions between the model's two regimes by using the BV approach. In the present study, we do not purport to carry out actual predictions: we merely highlight the zones on the attractor where the predictability is very low due to a possible regime change.

The equations of the Lorenz[44] model are given by

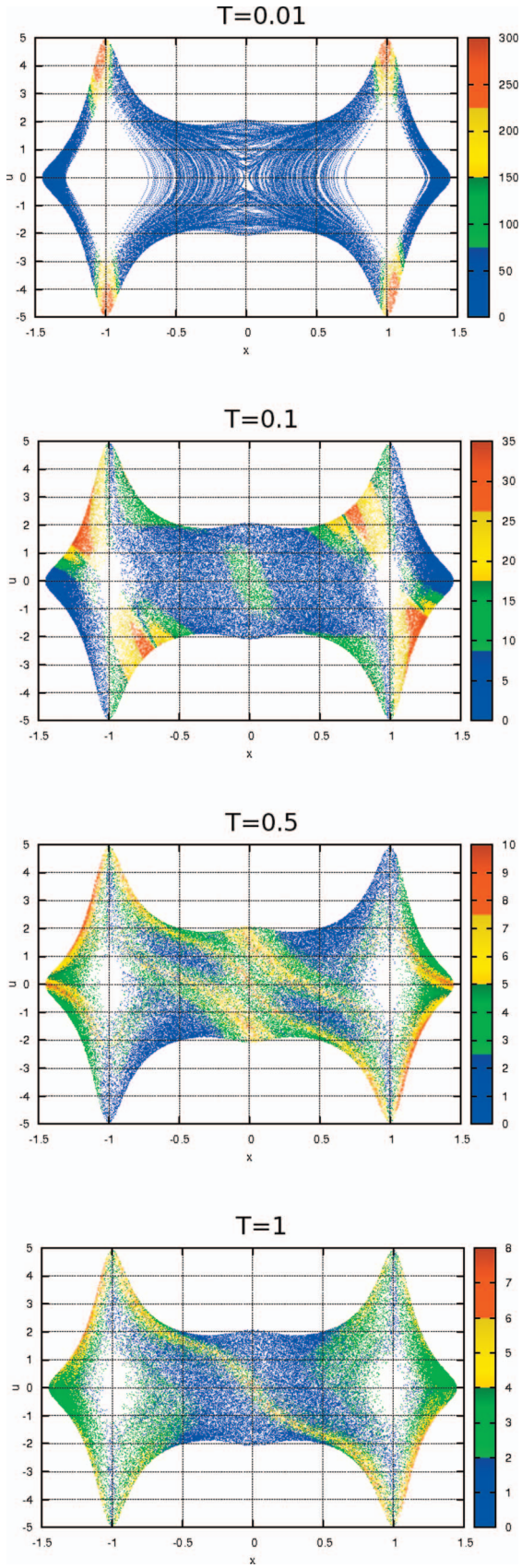


FIG. 10. (Color) Same as Fig. 6 for the coupled-particle system but using the SV approach only and with the renormalization times $T$ adapted to our coupled Hamiltonian oscillator. The plots are a projection onto the $(x_1, u_1)$ plane; panels are identified by the renormalization time $T$ used.

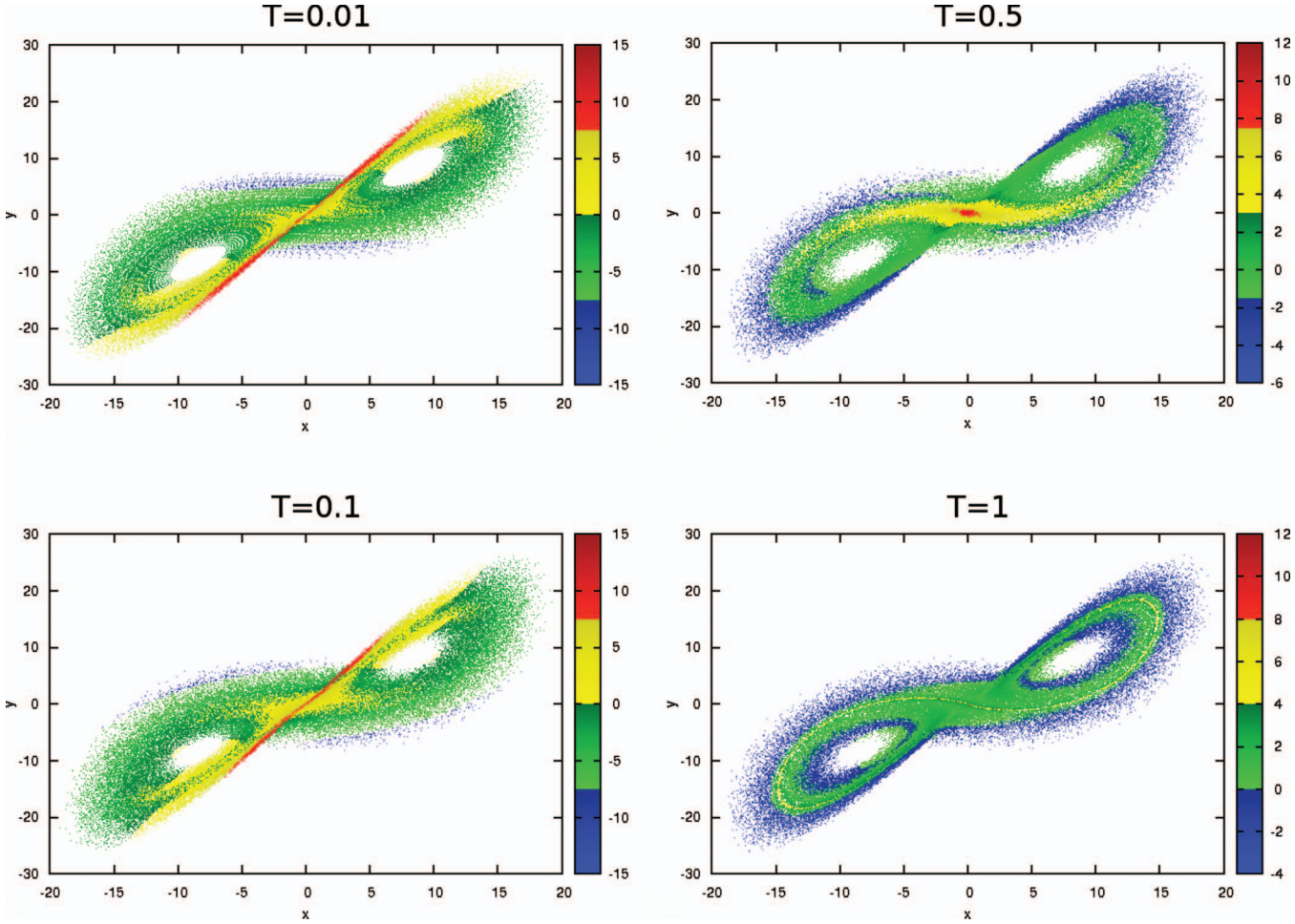


FIG. 11. (Color) Local Lyapunov exponent of the Lorenz (Ref. 44) model computed using the Gram–Schmidt method for different renormalization times $T$ and for $10^5$ points. The separatrix appears very clearly in this projection on the $(X,Y)$ plane; panels are identified by the renormalization time $T$.

$$\dot{X} = Pr(Y - X),$$

$$\dot{Y} = -XZ + rX - Y, \tag{C1}$$

$$\dot{Z} = XY - bZ,$$

and we use the canonical parameter values $Pr=10$, $b=8/3$, and $r=28$. Recall that, for these parameter values, the model has three unstable fixed points: the conductive one at the origin, $(X,Y,Z)=(0,0,0)$, and the two symmetrically placed convective ones, $(X,Y,Z)=(\pm X_0, \pm Y_0, Z_0)$, with $X_0=Y_0=(b(r-1))^{1/2}$ and $Z_0=r-1$.

We examine now the behavior of the first local Lyapunov exponent, computed using the Gram–Schmidt renormalization method. The results of our computations are plotted in Fig. 11 for different renormalization times $T$.

The first panel of Fig. 11 agrees quite well with Fig. 3 of Evans *et al.*,[21] except that their figure is a 3D perspective plot, while ours is a projection on the $(X,Y)$ plane. For small $T$, the leading Lyapunov vector and BV (not shown) coincide. Like in Appendix B, the zones with the most rapid error growth at low $T$ correspond to high-velocity zones on the attractor Once again, when we increase $T$, the zone of low predictability stretches and finally, when $T$ exceeds the duration of a small oscillation around either convective center—i.e., about 0.75 nondimensional time unit—this zone coincides with the neighborhood of the stable manifold of the conductive point.

The main conclusion from both appendixes is that any of the three methods of local predictability study—whether BVs, SVs, or local Lyapunov exponents—will show that the regions of lowest predictability for regime transitions align with the stable manifold of a centrally located point provided, that is, the renormalization time $T$ is long enough; in each case, $T$ should exceed the typical time scale of the dynamics within a regime. For large-scale, midlatitude LFV, this result, along with the CDV result in the main text, points to a $T$ that is longer than the one currently used in operational weather prediction and that equals or exceeds the typical life cycle of a baroclinic eddy of 5–7 days.

[1]Aurell, E., Boffetta, G., Crisanti, A., Paladin, G., and Vulpiani, A., "Predictability in the large: an extension of the concept of Lyapunov exponent," J. Phys. A **30**, 1–26 (1997).
[2]Barreira, L., in *Proceedings of the XIVth International Congress on Mathematical Physics* (World Scientific, Singapore, 2006), pp. 415–422.
[3]Benzi, R., P. Malguzzi, A. Speranza, and A. Sutera, "The statistical properties of the general atmospheric circulation: Observational evidence and a minimal theory of bimodality," Quart. J. Roy. Meteor. Soc. **112**, 661674 (1986).

[4]Bowman, K. P., "Manifold geometry and mixing in observed atmospheric flows", 1999 (unpublished); see also Bowman, K. P., Pan, L. L., Campos, T., and Gao, R., "Observations of fine-scale transport structure in the upper troposphere from the High-Performance Instrumented Airborne Platform for Environmental Research," J. Geophys. Res. **112**, D18111, doi:10.1029/2007JD008685 (2007).
[5]Buizza, R. and Palmer, T., "The singular vector structure of the atmospheric general circulation," J. Atmos. Sci. **52**, 1434–1456 (1993).
[6]Branstator, G., "Analysis of general circulation model sea-surface temperature anomaly simulations using a linear model. Part II: Eigenanalysis," J. Atmos. Sci. **42**, 2242–2254 (1985).
[7]Cai, M., Kalnay, E., and Toth, Z., "Bred Vectors of the Zebiak-Cane model and their potential application to ENSO predictions," J. Clim. **16**, 40–56 (2003).
[8]Charney, J. G. and Devore, J. G., "Multiple flow equilibria in the atmosphere and blocking," J. Atmos. Sci. **36**, 1205–1216 (1979).
[9]Charney, J. G. and Eliassen, A., "A numerical method for predicting the perturbations of the middle latitude westerlies," Tellus **1**, 38–54 (1949).
[10]Charney, J. G. and Straus, D. M., "Form-drag instability, multiple equilibria and propagating planetary waves in Baroclinic, orographically forced, planetary wave systems," J. Atmos. Sci. **37**, 1157–1176 (1980).
[11]Corti, S. and Palmer, T. N., "Sensitivity analysis of atmospheric low-frequency variability," Q. J. R. Meteorol. Soc. **123**, 2425–2447 (1997).
[12]Crommelin, D. T., "Homoclinic dynamics: A scenario for atmospheric ultralow-frequency variability," J. Atmos. Sci. **59**, 1533–1549 (2002).
[13]Crommelin, D. T., Opsteegh, J. D., and Verhulst, F., "A mechanism for atmospheric regime behavior," J. Atmos. Sci. **61**, 1406–1419 (2004).
[14]D'Andrea, F., "Extratropical low-frequency variability as a low-dimensional problem. Part II: Stationarity and stability of large-scale equilibria," Q. J. R. Meteorol. Soc. **128**, 1059–1073 (2001).
[15]D'Andrea, F. and Vautard, R., "Extratropical low-frequency variability as a low-dimensional problem. Part I: A simplified model," Q. J. R. Meteorol. Soc. **127**, 1357–1374 (2001).
[16]Deloncle, A., Berk, R., D'Andrea, F., and Ghil, M., "Weather regime prediction using statistical learning," J. Atmos. Sci. **64**, 1619–1635 (2007).
[17]DeSwart, H., "Analysis of a six-component atmospheric spectral model: chaos, predictability and vacillation," Physica D **36**, 222–234 (1989).
[18]DeSwart, H. E., and J. Grasman, "Effect of stochastic perturbations on a spectral model of atmospheric circulation," Technical Report, 1985.
[19]Dijkstra, H. A. and Ghil, M., "Low-frequency variability of the large-scale ocean circulation: A dynamical systems approach," Rev. Geophys. **43**, RG3002, doi:10.1029/2002RG000122 (2005).
[20]Doedel, E., A. Champneys, T. Fairgrieve, Y. Kuznetsov, B. Sandstede, and X. Wang, *AUTO97: Continuation and bifurcation software for ordinary differential equations*, 1997.
[21]Evans, E., Kalnay, E. *et al.*, "The Lorenz model is predictable," Bull. Am. Meteorol. Soc. **85**, 520–524 (2004).
[22]Ghil, M., "Hilbert problems for the geosciences in the 21st century," Nonlinear Processes Geophys. **8**, 211–222 (2001).
[23]Ghil, M. and Childress, S., *Topics in Geophysical Fluid Dynamics: Atmospheric Dynamics, Dynamo Theory and Climate Dynamics* (Springer-Verlag, New York, 1987).
[24]Ghil, M. and Robertson, A., "Waves vs. particles in the atmosphere's phase space: A pathway to long-range forecasting?," Proc. Natl. Acad. Sci. U.S.A. **99**, 2493–2500 (2002).
[25]Ghil, M. and Robertson, A. W., "Solving problems with GCMs: General circulation models and their role in the climate modeling hierarchy," in *General Circulation Model Development: Past, Present and Future* (Academic, New York, 2000), Chap. 10, pp. 285–325.
[26]Goldhirsch, I., Sulem, P.-L., and Orszag, S. A., "Stability and Lyapunov stability of dynamical systems: A differential approach and a numerical method," Physica D **27**, 311–337 (1987).
[27]Grassberger, P. and Procaccia, I., "Characterization of strange attractors," Phys. Rev. Lett. **50**, 346–349 (1983).
[28]Gyarmati, G., Szunyogh, I., and Patil, D. J., "Local predictability in a simple model of atmospheric balance," Nonlinear Processes Geophys. **10**, 183–196 (2003).
[29]Haller, G., "Finding finite-time invariant manifolds in two-dimensional velocity fields," Chaos **10**, 99–108 (2000).
[30]Hannachi, A. and Legras, B., "Simulated annealing and weather regimes classification," Tellus, Ser. A **47**, 955–973 (1995).
[31]Hide, R. and Mason, P. J., "Sloping convection in a rotating fluid," Adv. Phys. **24**, 47–100 (1975).
[32]Holloway, G. and Eert, J., "Intransitive multiple equilibria in eddy-active barotropic flows," J. Atmos. Sci. **44**, 2001–2005 (1987).
[33]Houtekamer, P. L., Lefaivre, L., Derome, J., Ritchie, H., and Mitchell, H. L., "A system simulation approach to ensemble prediction," Mon. Weather Rev. **124**, 1225–1242 (1996).
[34]Jiang, S., Jin, F.-F., and Ghil, M., "Multiple equilibria, periodic, and aperiodic solutions in a wind-driven, double-gyre, shallow-water model," J. Phys. Oceanogr. **25**, 764–786 (1995).
[35]Jin, F.-F. and Ghil, M., "Intraseasonal oscillations in the extratropics: Hopf bifurcation and topographic instabilities," J. Atmos. Sci. **47**, 3007–3022 (1990).
[36]Joseph, B. and Legras, B., "Relation between kinematic boundaries, stirring, and barriers for the Antarctic polar vortex," J. Atmos. Sci. **59**, 1198–1212 (2002).
[37]Kimoto, M. and Ghil, M., "Multiple flow regimes in the Northern Hemisphere winter. Part 1: Methodology and hemispheric regimes," J. Atmos. Sci. **50**, 2625–2643 (1993).
[38]Kondrashov, D., Ghil, M., Chen, J., and Berk, R., "Predicting weather regime transitions in Northern Hemisphere data sets," Clim. Dyn. **29**, 535–551 (2007).
[39]Kondrashov, D., Kravtsov, S., and Ghil, M., "Empirical mode reduction in a model of extratropical low-frequency variability," J. Atmos. Sci. **63**, 1859–1877 (2006).
[40]Landau, L. D. and Lifshitz, E. M., *Mechanics*, Course of Theoretical Physics, 2nd ed. (Pergamon, Oxford, 1969).
[41]Legras, B. and Ghil, M., "Persistent anomalies, blocking and variations in atmospheric predictability," J. Atmos. Sci. **42**, 433–471 (1985).
[42]Legras, B. and Vautard, R., *Predictability Seminar Proceedings* (European Center for Medium-Range Weather Forecasts, Reading, UK, 1995), pp. 141–156.
[43]Lorenz, E. N., "Empirical orthogonal functions and statistical weather prediction, Scientific Report 1, Statistical Forecasting Project," MIT, Cambridge, Mass. (Defense Doc. Center No. 110268), 49 pp., 1956.
[44]Lorenz, E. N., "Deterministic nonperiodic flow," J. Atmos. Sci. **20**, 130–141 (1963).
[45]Lorenz, E. N., "The mechanics of vacillation," J. Atmos. Sci. **20**, 448–465 (1963).
[46]Lorenz, E. N., "Atmospheric predictability as revealed by naturally occurring analogues," J. Atmos. Sci. **26**, 636–646 (1969).
[47]Lorenz, E. N., "On the existence of a slow manifold," J. Atmos. Sci. **43**, 1547–1557 (1986).
[48]Lorenz, E. N., "Regimes in simple systems," J. Atmos. Sci. **63**, 2056–2073 (2006).
[49]Lott, F., Robertson, A. W., and Ghil, M., "Mountain torques and Northern Hemisphere low-frequency variability: Part I: Hemispheric aspects," J. Atmos. Sci. **61**, 1259–1271 (2004).
[50]Lott, F., Robertson, A. W., and Ghil, M., "Mountain torques and Northern Hemisphere low-frequency variability. Part II: regional aspects," J. Atmos. Sci. **61**, 1272–1283 (2004).
[51]Lynch, P., The swinging spring: A simple model of atmospheric balance, in *Large-Scale Atmosphere-Ocean Dynamics* (Cambridge University Press, Cambridge, 2002), pp. 64–108.
[52]Madden, R. A. and Julian, P. R., "Detection of a 40–50 day oscillation in the zonal wind in the Tropical Pacific," J. Atmos. Sci. **28**, 702–708 (1971).
[53]Madden, R. A. and Julian, P. R., "Description of global-scale circulation cells in the tropics with a 40–50 day period," J. Atmos. Sci. **29**, 1109–1123 (1972).
[54]Majda, A. J., Franzke, C. L., Fischer, A., and Crommelin, D. T., "Distinct metastable atmospheric regimes despite nearly gaussian statistics: A paradigm model," Proc. Natl. Acad. Sci. U.S.A. **103**, 8309–8314 (2006).
[55]Marcus, S. L., Ghil, M., and Dickey, J. O., "The extratropical 40–day oscillation in the UCLA general circulation model. Part I: atmospheric angular momentum," J. Atmos. Sci. **51**, 1431–1446 (1994).
[56]Marcus, S. L., Ghil, M., and Dickey, J. O., "The extratropical 40–day oscillation in the UCLA general circulation model. Part II: Spatial structure," J. Atmos. Sci. **53**, 1993–2014 (1996).
[57]Michelangeli, P. A., Vautard, R., and Legras, B., "Weather regimes: recurrence and quasistationarity," J. Atmos. Sci. **52**, 1237–1256 (1995).
[58]Mo, K. and Ghil, M., "Cluster analysis of multiple planetary flow regimes," J. Geophys. Res. **93**, 10927–10952, doi:10.1029/JD093iD09p10927 (1988).
[59]Molteni, F., "Weather regimes and multiple equilibria," in *Encyclopedia of Atmospheric Sciences* (Academic, New York, 2003), pp. 2577–2586.
[60]Molteni, F., Buizza, R., Palmer, T. N., and Petroliagis, T., "The ECMWF

ensemble prediction system: methodology and validation," Q. J. R. Meteorol. Soc. **122**, 73–119 (1996).
[61]Namias, J., "The index cycle and its role in the general circulation," J. Atmos. Sci. **7**, 130–139 (1950).
[62]Oseledec, V. I., "A multiplicative ergodic theorem. Characteristic Lyapunov exponents of dynamical systems," Trudy Moskow Mat. Obshch. **19**, 179–210 (1968).
[63]Peña, M. and Kalnay, E., "Separating fast and slow modes in a coupled system," Nonlinear Processes Geophys. **11**, 319–327 (2004).
[64]Pfeffer, R. L. and Chiang, Y., "Two kinds of vacillation in rotating laboratory experiments," Mon. Weather Rev. **95**, 75–82 (1967).
[65]Philander, S., *El Niño, la Niña and the Southern Oscillation* (Academic, San Diego, 1989).
[66]Quon, C. and Ghil, M., "Multiple equilibria in thermosolutal convection due to salt-flux boundary conditions," J. Fluid Mech. **245**, 449–484 (1992).
[67]Quon, C. and Ghil, M., "Multiple equilibria and stable oscillations in thermosolutal convection at small aspect ratio," J. Fluid Mech. **291**, 33–56 (1995).
[68]Reinhold, B. B. and Pierrehumbert, R. T., "Dynamics of weather regimes: quasi-stationary waves and blocking," J. Atmos. Sci. **110**, 1105–1145 (1982).
[69]Rossby, C. G. *et al.*, "Relation between variations in the intensity of the zonal circulation of the atmosphere and the displacements of the semi-permanent centers of action," J. Mar. Res **2**, 38–55 (1939).
[70]Sardeshmukh, P. D., Compo, G. P., and Penland, C., "Changes of probability associated with El Niño," J. Clim. **13**, 4268–4286 (2000).
[71]Schneider, S. H. and Dickinson, R. E., "Climate modeling," Rev. Geophys. Space Phys. **12**, 447–493, doi:10.1029/RG012i003p00447 (1974).
[72]Simonnet, E., Ghil, M., Ide, K., Temam, R., and Wang, S., "Low-frequency variability in shallow-water models of the wind-driven ocean circulation. Part I: Steady-state solution," J. Phys. Oceanogr. **33**, 712–728 (2003).
[73]Simonnet, E., Ghil, M., Ide, K., Temam, R., and Wang, S., "Low-frequency variability in shallow-water models of the wind-driven ocean circulation. Part I: Time dependant solution," J. Phys. Oceanogr. **33**, 729–752 (2003).
[74]Smyth, P., Ide, K., and Ghil, M., "Multiple regimes in Northern Hemisphere height fields via mixture model clustering," J. Atmos. Sci. **56**, 729–752 (1999).
[75]Stephenson, D., Hannachi, A., and O'Neill, A., "On the existence of multiple climate regimes," Q. J. R. Meteorol. Soc. **130**, 583–605 (2004).
[76]Sura, P., Newman, M., Penland, C., and Sardeshmukh, P., "Multiplicative noise and non-qaussianity: A paradigm for atmospheric regimes?," J. Atmos. Sci. **62**, 1391–1409 (2005).
[77]Tian, Y., Weeks, E. R., Ide, K., Urbach, J. S., Baroud, C. N., Ghil, M., and Swinney, H. L., "Experimental and numerical studies of an eastward jet over topography," J. Fluid Mech. **438**, 129–157 (2001).
[78]Toth, Z. and Kalnay, E., "Ensemble forecasting at NMC: The generation of perturbations," Bull. Am. Meteorol. Soc. **74**, 2317–2330 (1993).
[79]Toth, Z. and Kalnay, E., "Ensemble forecasting at NCEP and the breeding method," Mon. Weather Rev. **125**, 3297–3319 (1997).
[80]Trevisan, A., "Statistical properties of predictability from atmospheric analogs and the existence of multiple flow regimes," J. Atmos. Sci. **52**, 3577–3592 (1995).
[81]Vautard, R. and Legras, B., "Invariant manifolds, quasi-geostrophy and initialization," J. Atmos. Sci. **43**, 565–584 (1986).
[82]Weeks, E. R., Tian, Y., Urbach, J. S., Ide, H. L., Swinney, K., and Ghil, M., "Transitions between blocked and zonal flows in a rotating annulus with topography," Science **278**, 1598–1601 (1997).
[83]Xue, Y., Cane, M. A., Zebiak, S. E., and Palmer, T. N., "Predictability of a coupled model of ENSO using singular vector analysis. Part II: Optimal growth and forecast skill," Mon. Weather Rev. **125**, 2057–2073 (1997).
[84]Yoden, S., "Bifurcation properties of a quasi-geostrophic barotropic, low-order model with topography," J. Meteorol. Soc. Jpn. **63**, 535–546 (1985).
[85]Zebiak, S. E. and Cane, M. A., "A model El Niño southern oscillation," Mon. Weather Rev. **115**, 2262–2278 (1987).